https://doi.org/10.1016/j.engstruct.2020.110789

A Magnetic Levitation-based Tristable Hybrid Energy Harvester for Scavenging Energy from Low-frequency Structural Vibration

X. Yang[a], **C. Wang**[a], **S.K. Lai**[a,b,*]

[a] *Department of Civil and Environmental Engineering, The Hong Kong Polytechnic University, Kowloon, Hong Kong, P.R. China*

[b] *Hong Kong Branch of National Rail Transit Electrification and Automation Engineering Technology Research Center, The Hong Kong Polytechnic University, Kowloon, Hong Kong, P.R. China*

Abstract

A magnetic levitation-based hybrid energy harvester is proposed in this work. The new harvester consists of a tri-stable nonlinearity-enhanced mechanism that not only enhances the energy transfer through resonant inter-well oscillations, and also offers a wider bandwidth under low-frequency excitation levels. This integrated unit that combines a slider-driven electromagnetic generator (EMG) and a sliding-mode triboelectric nanogenerator (TENG) can harness more energy from vibration motions, thus resulting in a higher power density. In this study, both theoretical modelling and experimental studies are presented to investigate the dynamic characterization of the mechanical design, in which only four outer magnets are deployed on a plane to establish a triple-well nonlinear behaviour. Magnetic forces of this harvester are calculated by the magnetizing current method and the formation of tri-stable potential wells in the dynamic system is verified by a bifurcation analysis. In addition, a prototype of the harvester is fabricated and tested by an electrodynamic shaker system. The results show that the prototype exhibits a frequency bandwidth of 3–8 Hz and generates an output power of 6.9 mW and 6.44 mW in both horizontal and vertical orientations at a frequency of 8 Hz and 1g acceleration, respectively. A performance study is also compared to show that the proposed technique can produce sufficient power output compared to other electromagnetic-triboelectric devices.

*Corresponding author. E-mail address: sk.lai@polyu.edu.hk

Keywords: Structural Vibration, Hybrid Energy Harvester, Magnetic Levitation, Tri-stable Nonlinearity, Electromagnetic Generator, Triboelectric Nanogenerator.

1. Introduction

With the increasing use of wireless sensors, self-powered electronics and micro-electro-mechanical systems [1–3] for various engineering applications, powering such devices by traditional electrochemical batteries is limited in lifespan, required periodic recharging and chemically hazardous. One viable solution is to directly harness energy from the sustainable environment, e.g., vibration energy. Recently, the race for different types of vibration-based energy harvesting techniques is keenly pursued for more energetic autonomy and higher working efficiency. Vibration-based energy harvesting techniques that are an attractive but complicated topic can generate electrical energy from kinetic motions. Due to the incorruptibility and sustainability of vibration energy from ambient sources, a myriad of mechanisms have been extensively exploited to harvest vibration energy, including piezoelectric [4–9], electromagnetic [10–18], electrostatic [19, 20] and triboelectric [21–29] approaches. Earlier efforts mainly focused on linear dynamic harvesters, which can only work in a very narrow bandwidth, i.e., when an external excitation is almost equal to the fundamental frequency of such dynamic systems. In real-world engineering conditions, structural vibration sources are often low-amplitude (< 1g), low-frequency (< 10 Hz) or time-varying in nature, e.g., power line aeolian vibration, wind turbine dynamics and train-track interaction. Under non-resonant oscillations, the performance of such harvesters is therefore rapidly degraded. Moreover, many energy harvesters are difficult to go into high-energy orbits under low-level excitations, such that the power output generated by a resonant generator decreases dramatically under low frequencies [30].

To address this issue, nonlinear energy harvesting technologies have been introduced to broaden the usable bandwidth of linear counterparts, including mono-stable, bi-stable and multi-stable oscillating mechanisms [31]. In mechanical and structural engineering, nonlinear dynamics is useful for explaining complicated phenomena in many low- and high-dimensional problems [32–36]. By creating more potential wells in a nonlinear dynamic system, its potential energy can be distributed more uniformly, thereby providing a shallower potential well and resulting in a lower excitation threshold for inter-well motions [37]. The intrinsic behaviour of triple-well nonlinear oscillators can be illustrated by Duffing-type equations [38–40]. In vibration-driven energy harvesting techniques, this nonlinear behavior can be achieved by using a repulsive or attractive magnetic harvester. These energy harvesting devices generally consist of a cantilever beam with

piezoelectric patches and a permanent magnet at its tip [37]. A tri-stable potentatal configuration can be triggered by two fixed magnets and its nonlinearity is induced by magnetic forces.

As aforementioned, another difficulty in conventional energy harvesting techniques is to generate energy from low-frequency vibration sources by using a single energy scavenging mechanism (e.g., either a piezoelectric approach or an electromagnetic approach). Due to their own unique qualities and limitations, the power generation of such vibration energy harvesters is very limited under low-level excitations. To harness more electrical energy under vibration motions and low-frequency sources, coupling multiple transduction mechanisms into a single unit is a superior solution. Motivated by this research idea, various coupling mechanisms, such as piezoelectric-electromagnetic [41–45], electromagnetic-triboelectric [46–52], piezoelectric-triboelectric [53–55] and even tribolelectic-thermoelectric [56, 57] generators, have been proposed. By hybridizing two transduction mechanisms, the advantages of different transduction mechanisms can be compacted into a unique module.

In the literature, there is a vast amount of information on piezoelectric-type energy harvesters. To compare with the performance of piezoelectric energy harvesters, electromagnetic energy harvesters are able to work under low-frequency conditions and can be produced with affordable expenses. Besides, such an energy harvester has a longer lifespan by using a magnetically levitated technique instead of mechanical springs that are easily worn out after a period of time. Making use of magnetic levitation techniques, Zhu and Zu [58] investigated a magnetoelectric harvester and presented the vibration amplitudes and energy output responses of the system. Mann and his associates [59, 60] not only provided the theoretical design of a magnetically levitated energy harvester, and also presented a bi-stable electromagnetic-induction energy generator via magnetic levitation oscillations. Soares dos Santos et al. [61] introduced a nonlinear model to study the energy transduction effect of a magnetic levitation-based electromagnetic energy harvesting technique. More recently, Gao et al. [62] presented an electromagnetic-induction energy harvester by using the magnetic levitation effect. Wang et al. [63] conducted a parametric analysis of using magnetic levitation for energy harvesting. Furthermore, Tan et al. [64] proposed a battery-like hybrid module based on magnetic levitation to harness energy from human motions.

Consider the effect of magnetic levitation, magnetic forces can be calculated using different analytical methods. The method of magnetic dipoles [65–67] is commonly used to consider all permanent magnets as point dipoles when the size of such magnets is sufficiently small compared

to the separation interval of that magnets. To consider the geometry and size of magnets, the magnetizing current method was used [68] to calculate magnetic forces acting on permanent magnets in the presence of external magnetic fields. Such a method enables to calculate the magnitude of magnetic forces, where the calculation model can be obtained by replacing those magnets with a suitable distribution of magnetizing currents. Employing this method, the dynamic behaviour of piezoelectric cantilever energy harvesting systems with a bi-stable potential well [69] and a tri-stable potential well [70] under magnetic fields can be calculated analytically. To compare with the method of magnetic dipoles, this calculation method is more applicable for different magnet intervals.

In this work, we propose a novel magnetic levitation-based electromagnetic-triboelectric energy harvester that can work well under low-frequency and low-amplitude sources. This harvester governed by the tri-stable nonlinearity-enhanced mechanism is realized by a simple arrangement of using four outer magnets on a plane. The tri-stable nonlinearity with resonant inter-well oscillations in a magnetically levitated structure can make the hybrid device possess a higher working efficiency and a wider operating bandwidth at low frequencies. The magnetizing current method [68] is applied to calculate the magnetic forces of this model to reveal the triple-well nonlinear phenomenon. The formation mechanism of the tri-stable nonlinear behavior is also investigated by a bifurcation analysis. To verify the theoretical model, a prototype of the harvester is fabricated for experimental studies. Under electrodynamical shaking tests, the output performance of the fabricated prototype is studied. To this end, the structure of this paper is organized as follows. Section 2 describes the design configuration, working principle, formation mechanism and theoretical analysis of the proposed system. In Section 3, experimental results are discussed to evaluate the performance of this hybrid energy harvester. Finally, major findings of the present work are summarized in Section 4.

2. System and Design

2.1 Design configuration of the hybrid generator

In this work, a slider-driven electromagnetic generator (EMG) and a sliding-mode triboelectric nanogenerator (TENG) were optimally integrated in a suspended structure via a magnetically levitated approach, as schematically illustrated in Fig. 1. Two parallel stainless steel rods as the framework of this hybrid generator were fixed by three sets of fasteners made up of aluminum

alloy. A cylindrical PVC tube (with a length of 37 mm) was attached at the middle fastener. Four cuboid neodymium magnets (NdFeB, $5\ \text{mm} \times 3\ \text{mm} \times 2\ \text{mm}$, N35 grade) were fixed to an outer sleeve around the PVC tube. The other two fasteners, each of them consisted of a micrometer and one NdFeB cylindrical magnet ($\phi 10\ \text{mm} \times 4\ \text{mm}$, N35 grade), were symmetrically placed at both sides of the PVC tube and separated by an adjustable distance from the tube. The micrometers can be used to fine-tune the design based on the theoretical analysis of this work to achieve a tri-stable nonlinear system. The EMG unit consisted of a series of copper coils and one NdFeB cylindrical magnet (moving magnet) ($\phi 12\ \text{mm} \times 18\ \text{mm}$, N35 grade) placed in the cylindrical PVC tube to restrain its motion in a single direction. The other two cylindrical magnets with their magnetic poles were oriented to repel the moving magnet, thereby rendering the suspension of the moving magnet inside the tube. The resultant magnetic force, combined with the interaction between the moving magnet and the four outer magnets, can create a tri-stable potential well in the system. Eight ring-shaped coils (with a total number of 1900 turns) were connected in series and wrapped over the PVC tube. For the TENG unit, a 50-μm-thick aluminum (Al) film covered the curved surface of the moving magnet as a freestanding tribo-material. Two 50-μm-thick copper (Cu) films were attached on the inner surface of the PVC tube with a 0.1-mm gap between them, which can serve as back electrodes. A 50-μm-thick polytetrafluoroethylene (PTFE) film was aligned onto the surfaces of the back electrodes as another tribo-material.

2.2 Working principle of the hybrid generator

When an external force is exerted on the hybridized system along the PVC tube, the moving magnet (as a proof mass) covered by an Al film can act as a slider to oscillate inside the tube. The sliding behavior can induce the coupling effect of the EMG and TENG units, see Fig. 2. The EMG unit works on Faraday's law: the change of rate of the magnetic flux through the coils develops an inductive electromotive force in the coils, as well as Lenz's law: the direction of induced voltage in the coils opposes the change of magnetic fields produced by it [71]. The electromagnetic output can be extracted directly from the coils. For the TENG unit, the Al electrode can generate friction during vibration modes. The internal surface of the tube was attached to a PTFE film with two Cu electrodes, which can be used to collect the power output. According to the triboelectric effect [21, 22], PTFE has a higher electron affinity than Al, this results in negative triboelectric charges on

the PTFE film surface and positive triboelectric charges on the Al surface during the direct contact of both surfaces.

Figure 3 shows a schematic diagram of the power generation process over a half cycle that can be divided into four stages. At the neutral position (stage i), the slider is at the center of the tube with equal negative charges on the two Cu electrodes. Once the slider moves to the right side of the tube (stage ii), the magnetic flux across the coils increases on the right side and decreases on the left. The current flow induced in the two coils by the electromagnetic induction is in opposite directions according to Lenz's law. Meanwhile, increasing the relative displacement between the slider and the PTFE film causes a different inductive potential between the two Cu electrodes, which drives inductive electrons to flow from the left electrode to the right one, forming a triboelectric current to the left. The electromagnetic and triboelectric currents last until the slider reaches its maximum relative displacement (stage iii). The slider is then pushed back with decreasing the relative displacement by the restoring force of the system (stage iv).

As the magnetic flux keeps changing across the coils, it can generate an EMG current opposite that of stage ii. Meanwhile, the potential difference between the two Cu electrodes decreases, and the induced electrons flow back from the right electrode to the left one, generating a triboelectric current to the right. The slider then returns to the initial state and repeats the process on the other side. In this way, the electromagnetic and triboelectric currents can be constantly generated by the proposed system.

2.3 Formation of tri-stable nonlinear behavior

A tri-stable nonlinear characteristic is designed in the proposed hybrid generator. This characteristic can be realized by the magnetic interaction. Figure 4 shows the configuration and its associated geometric parameters of the magnets. Both rectangular and cylindrical coordinate systems are set and the origins of them are located at the center of the moving magnet A. Two static cylindrical magnets (i.e., C1 and C2) are placed on the z axis. Four outer magnets, namely B1, B2, B3 and B4, are placed in the x-y plane. The magnetizing current method [68] is employed in the current magnet model. In this model, we concern the magnetic forces on the moving magnet (A) in the z direction due to the magnetic fields produced by the four outer magnets (B1, B2, B3 and B4) and two static cylindrical magnets (C1 and C2). For simplicity and brevity, they are

denoted by $F_{\text{B-z}}$ and $F_{\text{C-z}}$, respectively. According to the magnetizing current method, these two force components can be written as:

$$\vec{F}_{\text{B-z}} = \iint_S \vec{K}_m \times \vec{B}_{ext-B} dS \tag{1a}$$

$$\vec{F}_{C-z} = \iint_S \vec{K}_m \times \vec{B}_{ext-C} dS \tag{1b}$$

where $\vec{K}_m$ is the surface current density of the magnet A; $\vec{B}_{ext-B}$ and $\vec{B}_{ext-C}$ are the external magnetic flux densities of the magnets B1–B4 and C1–C2, respectively; S is the surface area of the magnet A; and $\vec{K}_m$ is given by

$$\vec{K}_m = \vec{m}_A \times \vec{n} \tag{2}$$

where $\vec{m}_A$ is the magnetization of the magnet A and $\vec{n}$ is a unit vector in the outward direction of the surface. The magnetization of the magnet A is in the *z* direction, so the magnetizing current densities $\vec{K}_m$ on the left and right surfaces of the magnet A are zero. On the curved surface of the magnet A, the direction of $\vec{K}_m$ is tangent to the cross section of the magnet A. For simplicity, the magnetic forces can be calculated using the cylindrical coordinate system with an origin at point O as shown in Fig. 4.

The magnetic flux density of an isotropic medium can be expressed by

$$\vec{B} = \mu \vec{H} \tag{3}$$

where μ is the magnetic permeability and $\vec{H}$ is the magnetic field strength. According to Eq. (1), it is not difficult to understand that only the magnetic field strength along the $\vec{r}$ direction needs to be considered in order to calculate the magnetic forces $F_{\text{B-z}}$ and $F_{\text{C-z}}$ in the z direction.

For a cuboidal magnet (length (*l*) × width (*w*) × height (*h*)) with a uniform magnetization M_0 in the *z*-direction at the origin of the rectangular coordinate system, the *x*- and *y*-components of the magnetic field strength at a point (x_0, y_0, z_0) are given by [68]:

$$H_{B-x}(x_0, y_0, z_0) = \frac{M_0}{4\pi} \sum_{k,m,n=1}^{2} (-1)^{k+m+n} \ln \left\{ y_0 + (-1)^n \frac{l}{2} + \sqrt{\left[x_0 + (-1)^k \frac{w}{2} \right]^2 + \left[y_0 + (-1)^m \frac{l}{2} \right]^2 + \left[z_0 + (-1)^n \frac{h}{2} \right]^2} \right\} \tag{4a}$$

$$H_{B-y}(x_0, y_0, z_0) = \frac{M_0}{4\pi} \sum_{k,m,n=1}^{2} (-1)^{k+m+n} \ln \left\{ x_0 + (-1)^n \frac{w}{2} + \sqrt{\left[x_0 + (-1)^k \frac{w}{2} \right]^2 + \left[y_0 + (-1)^m \frac{l}{2} \right]^2 + \left[z_0 + (-1)^n \frac{h}{2} \right]^2} \right\} \tag{4b}$$

For a cylindrical magnet (with a diameter of "2a" and a height of "2t") with a uniform magnetization M_0 in the z-direction at the origin, the r-component of the magnetic field strength at a point (ρ_0, θ_0, z_0) in the cylindrical coordinate system, using the Gaussian hypergeometric expression, is given by [72]:

$$H_{C-r}(\rho_0,\theta_0,z_0) = -\frac{M_0}{8}\sqrt{\frac{a}{2\rho_0}}\left\{\left[\left(\frac{2a\rho_0}{(z_0-1.5t)^2+\rho_0^2+a^2}\right)^{3/2} F\left(\frac{5}{4},\frac{3}{4};2;\left(\frac{2a\rho_0}{(z_0-1.5t)^2+\rho_0^2+a^2}\right)^2\right)\right]\right. \\ \left. -\left[\left(\frac{2a\rho_0}{(z_0-0.5t)^2+\rho_0^2+a^2}\right)^{3/2} F\left(\frac{5}{4},\frac{3}{4};2;\left(\frac{2a\rho_0}{(z_0-0.5t)^2+\rho_0^2+a^2}\right)^2\right)\right]\right\} \quad (5)$$

where F is the Gaussian hypergeometric function. Upon substituting Eqs. (3) – (5) into Eq. (1) with the cylindrical coordinate system in Fig. 4 yields,

$$F_{B-z}(s) = -4\mu\int_{-\frac{h_A}{2}+s}^{\frac{h_A}{2}+s}\int_0^{2\pi}\vec{K}_m\cdot\left(\vec{H}_{B-x}(R_A\cos\theta-R_B,R_A\sin\theta,z)\cos\theta+\vec{H}_{B-y}(R_A\cos\theta-R_B,R_A\sin\theta,z)\sin\theta\right)\cdot R_A d\theta dz \quad (6a)$$

$$F_{C-z}(s) = \mu\int_{-\frac{h_A}{2}+s}^{\frac{h_A}{2}+s}\int_0^{2\pi}\vec{K}_m\cdot\left(\vec{H}_{C-r}(R_A,\theta,d/2-z)-\vec{H}_{C-r}(R_A,\theta,d/2+z)\right)\cdot R_A d\theta dz \quad (6b)$$

where s is the relative displacement between the slider and the tube. We observe that the proposed energy harvester performs symmetric oscillations in a horizontal position due to the magnetic forces. While the proposed energy harvester is placed in a vertical position, under the magnetic interaction and the effect of gravity, the oscillating system becomes asymmetric. These two conditions are given below:

(a) *Symmetric system*

In this condition, the restoring force (F_r) is written as

$$F_r(s) = F_{B-z}(s) + F_{C-z}(s) \quad (7)$$

(b) *Asymmetric system*

In this case, the restoring force (F_r) becomes

$$F_r(s) = F_{B-z}(s) + F_{C-z}(s) + F_g \quad (8)$$

where F_{B-z} and F_{C-z} are given in Eq. (6), and F_g is the force of gravity.

In theoretical analysis, a bifurcation study around the equilibrium states of the nonlinear system is performed to examine the existence of a triple-well behavior based on the restoring forces given in Eqs. (7) and (8). Relevant parameters and values of the hybrid energy harvester are listed in Tables 1 and 2. Figure 5 depicts the bifurcation behavior for the equilibrium states of the symmetric

system with various distance values R_B = 10 mm, 11.5 mm and 16 mm, where R_B is the distance between the centers of the four outer magnets (B1, B2, B3 and B4) and the coordinate origin. In the figure, d is the distance between the centers of both cylindrical magnets (C1 and C2). The solid and dashed lines denote the stable and unstable equilibria, respectively. When R_B is relatively small (R_B = 10 mm and 11.5 mm), the oscillator exhibits a mono-stable system with one stable trivial equilibrium only when $d < d_A$ (distance at point A). Increasing the value of d, a pair of saddle-node bifurcation points (at point A) occur to form a tri-stable oscillator with two unstable non-trivial equilibria and three (non-)trivial stable equilibria. Further increasing the value of d leads the system to a bi-stable oscillator when it passes through the pitchfork bifurcation point B where the trivial stable equilibria become unstable. When R_B reaches to 16 mm, as depicted in Fig. 5(c), a pair of pitchfork bifurcation points disappear and the tri-stable region vanishes as well.

Potential energy diagrams governed by different values of d for R_B = 10 mm, 11.5 mm and 16 mm are presented in Fig. 6. As d increases, the oscillator, with R_B = 10 mm or 11.5 mm, changes from a mono-stable state to a tri-stable state, and further to a bi-stable state. In the tri-stable state, the depth of the outmost two symmetric potential wells decreases as d increases, which makes the large-amplitude inter-well motion harder to achieve since it is more difficult to escape from the outmost wells. At R_B = 16 mm, when d increases, the oscillator changes from a mono-stable state to a bi-stable state and the depth of the two symmetric potential wells goes deeper in the bi-stable state. Especially, when d = 53.2 mm in Fig. 5(a) and d = 58.5 mm in Fig. 5(b), the potential depth is more uniform with a lower potential barrier when comparing to other cases. Such potential shapes make the system achieve a large-amplitude inter-well motion more easily. A comparison of a tri-stable system and a mono-stable state (without the magnets B1, B2, B3 and B4) is given in Fig. 7. It is obvious that the potential with R_B = 11.5 mm and d = 58.5 mm requires less kinetic energy to excite a large displacement motion. In the experimental test (horizontal orientation), this configuration of the system is employed for the proposed energy harvester to harness energy under low-level excitations.

In Fig. 8(a), the bifurcation behavior for the equilibrium states of the asymmetric system for R_B = 10 mm is plotted. The solid and dashed lines denote the stable and unstable equilibria, respectively. The oscillator exhibits a mono-stable system with one stable equilibrium when $d < d_A$. Increasing the value of d, a saddle-node bifurcation point (at point A) occurs to form a bi-stable oscillator with one unstable equilibria and two stable equilibria. Further increasing the value of d

leads the system to a tri-stable oscillator when a saddle-node bifurcation point B occurs. The generator finally becomes a bi-stable system at a saddle-node bifurcation point C.

Figure 8(b) shows the potential energy diagram under different values of d for R_B = 10 mm. As d increases, the oscillator changes in the sequence of: a mono-stable state → a bi-stable state → a tri-stable state. In the tri-stable state (when d = 52.5 mm), it is quite difficult for the system to escape from the middle well to the left well due to a higher potential barrier. The twofold-well potential (when d = 50.5 mm) has a uniform depth and a lower potential barrier, resulting in a much lower excitation threshold for inter-well motions. Therefore, in the following experimental test (vertical alignment), this bi-stable configuration of the system is employed for the proposed energy harvester to harness energy under low-level excitations.

2.4 Theoretical modeling of the proposed system

A lumped parameter mechanical model of the hybrid energy harvester under a base excitation along the axial direction is shown in Fig. 9(a). The governing equation of the system is expressed by

$$m\ddot{x} + c\dot{x} + F_r(x) + f_d = -m\ddot{z}_b \tag{9}$$

where m is the proof mass, c is the total damping coefficient (including mechanical and electrical damping), f_d is the dry friction between the Al and PTFE films, $\ddot{z}_b$ is the input base acceleration, x is the relative displacement of the moving magnet, and $F_r(x)$ is the nonlinear restoring force of the proposed energy harvester that can be calculated by either Eq. (7) or Eq. (8).

For the EMG unit, according to Faraday's Law, the open-circuit voltage V_{oc-EMG} and the short-circuit current I_{sc-EMG} are expressed as

$$V_{oc-EMG} = -N\, d\phi/dt \tag{10a}$$

$$I_{sc-EMG} = V_{oc}/R_l \tag{10b}$$

where N, ϕ and R_l are the number of coil turns, the magnetic flux through the area enclosed by the coils, and the total internal coil resistance of the coils, respectively.

For the TENG unit, the open-circuit voltage $V_{oc-TENG}$ and the short-circuit current $I_{sc-TENG}$ are given by

$$V_{oc-TENG} = Q_{sc}/C = \Delta S \cdot \sigma / C \tag{11a}$$

$$I_{sc-TENG} = dQ_{sc}/dt \tag{11b}$$

where Q_{sc}, C, and σ are the short-circuit transferred charge, the capacitance between two electrodes, and the surface charge density on the slider, respectively. Because the transferred charge is induced by the triboelectric charge on the slider, the potential difference between the two electrodes is proportional to the charge of contact area, ΔS.

A standard charging circuit for the hybrid energy harvester is presented in Fig. 9(b). To avoid the problem of internal power consumption, two full-wave bridge rectifiers are separately connected to the generators (EMG and TENG) to rectify the voltage outputs from AC to DC. The resultant DC outputs are then connected to a capacitor/load in parallel. Using this electronic circuit, the voltage outputs of both mechanisms in opposite phase can be circumvented.

3. Experimental studies

3.1 Shaker test setup

An experimental setup for the vibration test of the hybrid energy harvester is shown in Fig. 10. A waveform generator (KEYSIGHT 33500B) was used to generate signals to a power amplifier (APS 125) that can activate a long stroke vibration shaker (APS 113). Various excitation levels were measured by an accelerometer (DPO4104B) mounted on the shaking plate. All sampling signals were recorded and displayed on a digital oscilloscope (KEYSIGHT DSOX3014T). The hybrid energy harvester was mounted onto the shaking plate and the oscillation study was conducted in both horizontal and vertical directions, this can either eliminate or incorporate the effect of gravity.

3.2 Results and discussion

3.2.1 Experimental results in a horizontal direction

To characterize the output performance of the fabricated hybrid device, we measured the open-circuit peak-to-peak voltage of each unit (EMG and TENG) in the frequency range of 3–20 Hz under various excitation levels (0.3g, 0.6g and 1g), as shown in Fig. 11. At 0.3g, both generators can produce a large peak-to-peak open-circuit voltage at low frequencies around 4 Hz due to the resonant inter-well oscillations. Increasing the excitation frequency, the output voltage would drop at around 5 Hz and the generators exhibit a non-resonant behavior. When the excitation amplitude increased to 0.6g, the effect of frictional damping resulted in a small decrease of the voltage response at low frequencies. The generators can cover a continuous bandwidth of 3–7 Hz. When

the excitation amplitude further tuned to 1g, the frequency range of the resonant inter-well oscillations can work under 3–8 Hz.

In contrast, the measured open-circuit peak-to-peak voltage of the mono-stable counterpart without the magnets (B1, B2, B3 and B4) is shown in Fig. 12. The peak-to-peak open-circuit voltage can reach the highest values at about 12 Hz due to the effect of resonant oscillations, but the voltage would sharply drop at both sides of the resonant frequency. Hence, the tri-stable system can provide a wider operating bandwidth under low frequencies. In Fig. 13, the open-circuit voltage values of the EMG and TENG units under two excitation levels (7 Hz at 0.6g and 8 Hz at 1g) are presented. The results show that the peak-to-peak open-circuit voltage values of the EMG unit were 4.02 and 4.5 V, respectively. While for the TENG unit, the peak-to-peak open-circuit voltage values were 32.6 V and 35.4 V, respectively.

In addition to investigate the open-circuit voltage for electro-mechanical characterization, the maximum output power values of the EMG and TENG units were measured across different external loads at 8 Hz under 1g acceleration. As depicted in Fig. 14, for the EMG unit, a maximum power of 6.9 mW was obtained under an optimum load resistance of 42 Ω. By contrary, the TENG unit can produce a much higher open circuit voltage and a lower output power than those of the EMG unit due to a high internal impedance. The corresponding maximum power was 2.27 μW under a matching load resistance of 15 MΩ.

3.2.2 Experimental results in a vertical position

To study the effect of gravity on the prototype, the measured peak-to-peak open-circuit voltage of each unit in the frequency range of 3–20 Hz under various acceleration levels (0.3g, 0.6g and 1g) is illustrated in Fig. 15. At 0.3g, the generators can produce a large peak-to-peak open-circuit voltage at low frequencies around 4 Hz, this is mainly caused by the resonant inter-well oscillations. With the increase of excitation frequency, the output voltage would drop at around 5 Hz due to the effect of frictional damping and the occurrence of chaotic behavior at around 9 Hz. When the excitation amplitude increased to 0.6g and 1g, the effect of frictional damping only resulted in a decrease of the voltage responses at around 7 Hz. In these two cases, the occurrence of chaotic behavior was at 10–15 Hz. In short, the device can cover the frequency range of 3–6 Hz. Careful examination of Fig. 15 revealed the existence of chaotic regions (i.e., the vertical dots in red, blue and green colors) under various excitation levels.

In Fig. 16, under 8 Hz and 1g, the results showed that the peak-to-peak open-circuit voltages of the EMG and TENG units were about 3.82 V and 24.1 V, respectively. In this bi-stable system, the maximum output power values of the EMG and TENG units across different external load resistance at 8 Hz under 1g are shown in Fig. 17. The open circuit voltage is proportional to the load resistance. For the EMG unit, a maximum power of 6.44 mW was obtained under a matching load resistance of 41 Ω. For the TENG unit, the maximum power was 1.14 μW under a matching load resistance of 15 MΩ.

3.2.3 Performance comparison

A performance comparison between the proposed hybrid energy harvester and various electromagnetic-triboelectric energy harvesters is presented in Table 3. The comparison shows that the proposed hybrid energy harvester exhibits good performance in terms of the operation bandwidth and power density. In Fig. 18, simple demonstrations were also conducted to show that the present device can power three portable electronic humidity/temperature meters simultaneously in both horizontal and vertical orientations under 8 Hz and 1g.

It is worth noting that the focus of this research mainly undertakes the dynamic characterization of the proposed system to show the existence of tri-stable potential wells, which can broaden the operating bandwidth of the hybrid energy harvester under low frequencies. The power output of this design can be further enhanced by optimizing the governing parameters. This research is of importance in terms of both theoretical analysis and practical implication. The compact design of this battery-shaped device will foster many spin-off engineering applications and realize self-powered structural monitoring systems, because it can scavenge energy from low-frequency as well as low acceleration vibration sources, e.g., automobile transportation, railway vehicles, highway bridges and building motions. Moreover, a series of packs (similar to a battery pack with identical number of batteries) [64] can be used to support various power levels of low-energy electronics for structural monitoring. Furthermore, the implementation of a magnetic levitation approach in the present technique can reduce the possibility of mechanical contact and impact damage, thus ensuring long-term durability for practical use.

4. Conclusions

In this work, we designed a novel magnetic levitation-based hybrid energy harvester that can perform well under low-intensity and low-frequency sources. To faciliate the energy transfer, a tri-stable nonlinearity-enhanced mechanism was implemented. Key findings of the research are summarized below:

- A tri-stable nonlinear behavior was realized by using four outer static magnets on the same plane. Besides, a bifurcation analysis was conducted to identify the stable regime of the present system.
- Coupling the tri-stable nonlinear behavior to the system not only can provide a wider operating bandwidth under low-frequency excitation levels, and also increase the output performance via resonant inter-well oscillations.
- To examine the performance of the proposed design, experiments were carried out to demonstrate that the fabricated prototype can work well under a broadband range at 3–8 Hz.
- In the horizontal setup (without the effect of gravity), under 8 Hz and 1g, the EMG unit can deliver a peak output power of 6.9 mW across a loading resistance of 42 Ω, while the TENG unit can produce an output power of 2.27 μW across a loading resistance of 15 MΩ.
- In the vertical situation (under the effect of gravity), the fabricated prototype can produce a total power output of 6.44 mW under 8 Hz and 1g.
- Simple demonstrations were also conducted to indicate that sufficient power can be generated by the hybrid energy harvester to portable electronic devices.

Acknowledgements

The work described in this paper was supported by the Early Career Scheme (Project No. PolyU 252026/16E) and the Research Impact Fund (Project No. R5020-18) from the Research Grants Council of the Hong Kong Special Administrative Region. The funding support from the Innovation and Technology Commission of the HKSAR to the Hong Kong Branch of National Rail Transit Electrification and Automation Engineering Technology Research Center (K-BBY1) is also gratefully acknowledged.

References

[1] M. Shirvanimoghaddam, K. Shirvanimoghaddam, M.M. Abolhasani, M. Farhangi, Towards a green and self-powered Internet of Things using piezoelectric energy harvesting, IEEE Access, 7 (2019) 94533–94556.

[2] A.Z. Hajjaj, N. Jaber, S.Ilyas, F.K. Alfosail, M.I. Younis, Linear and nonlinear dynamics of micro and nanoresonators: Review of recent advances, Int. J. Non-Linear Mech., 119 (2020) 103328.

[3] J. Feng, C. Liu, W. Zhang, J. Han, S. Hao, Mechanical behaviors research and the structural design of a bipolar electrostatic actuation microbeam resonator, Sensors 19, ID1348, 2019.

[4] D. Castagnetti, Design and characterization of a fractal-inspired multi-frequency piezoelectric energy converter, Fracture and Structural Integrity, 23 (2013) 87–93.

[5] D. Castagnetti, E. Radi, A piezoelectric based energy harvester with dynamic magnification: modelling, design and experimental assessment, Meccanica, 53 (2018) 2725–2742.

[6] A. Keshmiri, N. Wu, Q. Wang, A new nonlinearly tapered FGM piezoelectric energy harvester, Eng. Struct. 173 (2018) 52–60.

[7] C. Wang, Q.C. Zhang, W. Wang, J.J. Feng, A low-frequency, wideband quad-stable energy harvester using combined nonlinearity and frequency up-conversion by cantilever-surface contact, Mech. Syst. Signal Process. 112 (2018) 305–318.

[8] S.K. Lai, C. Wang, L.H. Zhang, A nonlinear multi-stable piezomagnetoelastic harvester array for low-intensity, low-frequency, and broadband vibrations, Mech. Syst. Signal Process. 122 (2019) 87–102.

[9] W. Chen, Z.Y. Xiang, J.L. Mo, Z.Y. Fan, H.H. Qian, J.Y. Wang, Energy harvesting and vibration reduction by sandwiching piezoelectric elements into elastic damping components with parallel-grooved structures, Compos. Struct. 241 (2020) 112105.

[10] S. Zhu, W.A. Shen, Y.L. Xu, Linear electromagnetic devices for vibration damping and energy harvesting: Modelling and testing, Eng. Struct. 34 (2012) 198–212.

[11] G. Garuso, G. Chirianni, G. Vairo, Energy harvesting from wind-induced bridge vibrations via electromagnetic transduction, Eng. Struct. 115 (2016) 118–128.

[12] D. Castagnetti, A Belleville-spring-based electromagnetic energy harvester, Smart Mater. Struct., 24 (2015) 1–15.

[13] D. Castagnetti, F. Dallari, Design and experimental assessment of an electromagnetic energy harvester based on slotted disc-springs, Proc. Inst. Mech. Eng. Pt. L-J. Mater.-Design Appl., 231 (2017) 89–99.

[14] M. Yuan, K. Liu, A. Sadhu, Simultaneous vibration suppression and energy harvesting with a non-traditional vibration absorber, J. Intell. Mater. Syst. Struct. 29 (2018) 1748–1763.

[15] C.N. Loong, C.C. Chang, E.G. Dimitrakopoulos, Circuit nonlinearity effect on the performance of an electromagnetic energy harvester-structure system, Eng. Struct. 173 (2018) 449–459.

[16] D. Castagnetti, A simply tunable electromagnetic pendulum energy harvester, Meccanica, 54 (2019) 749–760.

[17] B. Yan, S. Zhou, C. Zhao, K. Wang, C. Wu, Electromagnetic energy harvester for vibration control of space rack: Modeling, optimization, and analysis, J. Aerosp. Eng 32 (2019) 04018126.

[18] Q. Cai, S. Zhu, Unified strategy for overall impedance optimization in vibration-based electromagnetic energy harvesters, Int. J. Mech. Sci., 165 (2020) 105198.

[19] L.G.W. Tvedt, D.S. Nguyen, E. Halvorsen, Nonlinear behavior of an electrostatic energy harvester under wide- and narrowband excitation, J. Microelectromech. Syst. 19 (2010) 305–316.

[20] Y. Lu, F. Cottone, S. Boisseau, A nonlinear MEMS electrostatic kinetic energy harvester for human-powered biomedical devices, Appl. Phys. Lett. 107 (2015) 253902.

[21] F. Fan, Z. Tian, Z.L. Wang, Flexible triboelectric generator, Nano Energy 1 (2012) 328–334.

[22] Z.L. Wang, Triboelectric nanogenerators as new energy technology for self-powered systems and as active mechanical and chemical sensors, ACS Nano 7 (2013) 9533–9557.

[23] S. Wang, L. Lin, Y. Xie, Q. Jing, S. Niu, Z.L. Wang, Sliding-triboelectric nanogenerators based on in-plane charge-separation mechanism, Nano Lett. 13 (2013) 2226–2233.

[24] W. Yang, J. Chen, Q. Jing, J. Yang, X. Wen, Y. Su, G. Zhu, P. Bei, Z.L. Wang, 3D stack integrated triboelectric generator for harvesting vibration energy, Adv. Funct. Mater. 24 (2014) 4090–4096.

[25] K. Parida, V. Kumar, W. Jiangxin, V. Bhavanasi, R. Bendi, P.S. Lee, Highly transparent, stretchable, and self-healing ionic-skin triboelectric nanogenerators for energy harvesting and touch applications, Adv. Mater. 29 (2017) 1702181.

[26] Z.L. Wang, T. Jiang, L. Xu, Toward the blue energy dream by triboelectric nanogenerator networks, Nano Energy 39 (2017) 9–23.

[27] D. Kim, S. Lee, Y. Ko, C.H. Kwon, J. Cho, Layer-by-layer assembly-induced triboelectric nanogenerators with high and stable electric outputs in humid environments, Nano Energy 44 (2018) 228–239.

[28] C. Park, S. Yu, S.M. Cho, G. Song, Y. Lee, H.S. Kang, S.W. Lee, H. Eoh, C. Park, Triboelectric nanogenerators with transfer-printed arrays of hierarchically de-wetted microdroplets, Nano Energy 51 (2018) 588–596.

[29] H. Guo, X. Pu, J. Chen, Y. Meng, M.H. Yeh, G. Liu, Q. Tang, B. Chen, D. Liu, Song Qi, C. Wu, C. Hu, J. Wang, Z.L. Wang, A highly sensitive, selfpowered triboelectric auditory sensor for social robotics and hearing aids, Sci. Robot. 3 (2018) eaat2516.

[30] R.L. Harne, K.W. Wang, A review of the recent research on vibration energy harvesting via bistable systems, Smart Mater. Struct. 22 (2013) 023001.

[31] M.F. Daqaq, R. Masana, A. Erturk and D.D. Quinn, On the role of nonlinearities in vibratory energy harvesting: A critical review and discussion, Appl. Mech. Rev., 66 (2014) 040801.

[32] W. Zhang, Y.Z. Liu, M.Q. Wu, Theory and experiment of nonlinear vibrations and dynamic snap-through phenomena for bi-stable asymmetric laminated composite square panels under foundation excitation, Compos. Struct., 225 (2019) 111140.

[33] M.H. Yao, L. Ma, W. Zhang, Study on power generations and dynamic responses of the bistable straight beam and the bistable L-shaped beam, Sci. China-Technol. Sci 61 (2018) 1404–1416.

[34] R.Q. Wu, W. Zhang, M.H. Yao, Nonlinear dynamics near resonances of a rotor-active magnetic bearings system with 16-pole legs and time varying stiffness, Mech. Syst. Signal Process. 100 (2018) 113–134.

[35] W. Zhang, X.P. Zhan, Periodic and chaotic motions of a rotor-active magnetic bearing with quadratic and cubic terms and time-varying stiffness, Nonlinear Dyn., 41 (2005) 331–359.

[36] S.K. Lai, C.W. Lim, Nonlinear vibration of a two-mass system with nonlinear stiffnesses, Nonlinear Dyn., 49 (2007) 233 – 249.

[37] C. Wang, S.K. Lai, Z.C. Wang, J.M. Wang, W.Q. Yang, Y.Q. Ni, A low-frequency, broadband and tri-hybrid energy harvester with septuple-stable nonlinearity-enhanced

mechanical frequency up-conversion mechanism for powering portable electronics, Nano Energ. 64 (2019) 103943.

[38] M. Siewe Siewe, H. Cao, M.A.F. Sanjuán, On the occurrence of chaos in a parametrically driven Rayleigh oscillator with three-well potential, Chaos Solitons Fractals, 41(2009) 772-782.

[39] I. Kovacic, M.J. Brennan, The Duffing Equation: Nonlinear oscillators and their behaviour, Wiley, 2011.

[40] S.K. Lai, X. Yang, F.B. Gao, Analysis of large-amplitude oscillations in triple-well non-natural systems, J. Comput. Nonlinear Dyn., 14 (2019) 091002.

[41] U. Javed, A. Abdelkefi, Role of the galloping force and moment of inertia of inclined square cylinders on the performance of hybrid galloping energy harvesters, Appl. Energy 231 (2018) 259–276.

[42] H. Rawnak, R.Y. Mehmet, A wearable energy harvester unit using piezoelectric-electromagnetic hybrid technique, Sens. Actuators 257 (2017) 198–207.

[43] R. Sriramdas, R. Pratap, An experimentally validated lumped circuit model for piezoelectric and electrodynamic hybrid harvesters, IEEE Sens. J. 18 (2018) 2377–2384.

[44] K.Q. Fan, S.H. Liu, H.Y. Liu, Y.M. Zhu, W.D. Wang, D.X. Zhang, Scavenging energy from ultra-low frequency mechanical excitations through a bi-directional hybrid energy harvester, Appl. Energy 216 (2018) 8–20.

[45] R.M. Toyabur, M. Salauddin, H. Cho, J.Y. Park, A multimodal hybrid energy harvester based on piezoelectric-electromagnetic mechanisms for low-frequency ambient vibrations, Energy Convers. Manag. 168 (2018) 454–466.

[46] R.K. Gupta, Q. Shu, L. Dhakar, T. Wang, C.H. Heng, C. Lee, Broadband energy harvester using non-linear polymer spring and electromagnetic/triboelectric hybrid mechanism, Sci. Rep. 7 (2017) 41396.

[47] L. Jin, J. Chen, B.B. Zhang, W.L. Deng, L. Zhang, H.T. Zhang, X. Huang, M.H. Zhu, W.Q. Yang, Z. L. Wang, Self-powered safety helmet based on hybridized nanogenerator for emergency, ACS Nano 10 (2016) 7874-7881.

[48] M.L. Seol, J.W. Han, S.J. Park, Hybrid energy harvester with simultaneous triboelectric and electromagnetic generation from an embedded floating oscillator in a single package, Nano Energy 23 (2016) 50–59.

[49] M.L. Seol, S.B. Jeon, J.W. Han, Y.K. Choi, Ferrofluid-based triboelectric-electromagnetic hybrid generator for sensitive and sustainable vibration energy harvesting, Nano Energy 31 (2017) 233–238.

[50] J.X. Zhu, A.C. Wang, H.B. Hu, H. Zhu, Hybrid electromagnetic and triboelectric nanogenerators with multi-impact for wideband frequency energy harvesting, Energies 10 (2017) 2024.

[51] Md Salauddin, R.M. Toyabur, P. Maharjan, M.S. Rasel, J.W. Kim, H. Cho, J.Y. Park, High performance human-induced vibration driven hybrid energy harvester for powering portable electronics, Nano Energy 45 (2018) 236–246.

[52] Z. Saadatnia, E. Esmailzadeh, H.E. Naguib, Design, simulation, and experimental characterization of a heaving triboelectric-electromagnetic wave energy harvester, Nano Energy 50 (2018) 281–290.

[53] S.C. Karumuthil, S.P. Rajeev, S. Varghese, Piezo-tribo nanoenergy harvester using hybrid polydimethyl siloxane based nanocomposite, Nano Energy 40 (2017) 487–494.

[54] Y.B. Guo, X.S. Zhang, Y. Wang, W. Gong, Q.H. Zhang, H.Z. Wang, J. Brugger, All-fiber hybrid piezoelectric-enhanced triboelectric nanogenerator for wearable gesture monitoring, Nano Energy 48 (2018) 152–160.

[55] Z.J. Li, Z. Saadatnia, Z.B. Yang, H. Naguib, A hybrid piezoelectric-triboelectric generator for low-frequency and broad-bandwidth energy harvesting, Energy Convers. Manag. 174 (2018) 188–197.

[56] M.K. Kim, M.S. Kim, S.E. Jo, Y.J. Kim, Triboelectric-thermoelectric hybrid nanogenerator for harvesting frictional energy, Smart Materials and Structures, 25 (2016) 125007.

[57] Y. Wu, S. Kuang, H. Li, H. Wang, R. Yang, Y. Zhai, G. Zhu, Z.L. Wang, Triboelectric-thermoelectric hybrid nanogenerator for harvesting energy from ambient environments, Advanced Materials Technologies, 3 (2018) 1800166.

[58] Y. Zhu, J.W. Zu, A magneto electric generator for energy harvesting from the vibration of magnetic levitation, IEEE Trans. Magn. 48 (2012) 3344–3347.

[59] B.P. Mann, N.D. Sims, Energy harvesting from the nonlinear oscillations of magnetic levitation, J. Sound Vibr. 319 (2009) 515–530.

[60] B.P. Mann, B.A. Owens, Investigations of a nonlinear energy harvester with a bistable potential well, J. Sound Vibr. 329 (2010) 1215–1226.

[61] M.P. Soares dos Santos, J.A.F. Ferreira, J.A.O. Simões, R. Pascoal, J. Torrão, X. Xue, E.P. Furlani, Magnetic levitation-based electromagnetic energy harvesting: A semi-analytical nonlinear model for energy transduction, Sci. Reports, 6, 18579, 2016.

[62] M.Y. Gao, Y. Wang, Y.T. Wang, P. Wang, Experimental investigation of non-linear multi-stable electromagnetic-induction energy harvesting mechanism by magnetic levitation oscillation, Applied Energy 220 (2018) 856–876.

[63] Z. Wang, H. Feng, H. Ding, L. Chen, Parametric influence on energy harvesting of magnetic levitation using harmonic balance method, J. Vib. Eng. Technol., 7 (2019) 543–549.

[64] P. Tan, Q. Zheng, Y. Zou, B. Shi, D. Jiang, X. Qu, H. Ouyang, C. Zhao, Y. Cao, Y. Fan, Z.L. Wang, Z. Li, A battery-like self-charge universal module for motional energy harvest, Adv. Energy Mater., 9, 1901875, 2019.

[65] H. Li, W. Qin, C. Lan, W. Deng, Z. Zhou, Dynamics and coherence resonance of tri-stable energy harvesting system, Smart Mater. Struct. 25 (2016) 015001.

[66] P. Zhu, X. Ren, W. Qin, Z. Zhou, Improving energy harvesting in a tri-stable piezomagnetoelastic beam with two attractive external magnets subjected to random excitation, Arch Appl. Mech, 87 (2017) 45–57.

[67] C. Wang, Q.C. Zhang, W. Wang, Low-frequency wideband vibration energy harvesting by using frequency-up conversion and quin-stable nonlinearity, J. Sound Vibr. 399 (2017) 169–181.

[68] J.S. Agashe, D.P. Arnold, A study of scaling and geometry effects on the forces between cuboidal and cylindrical magnets using analytical force solutions, J. Phys. D: Appl. Phys. 41 (2008) 105001.

[69] D. Tan, Y.G. Leng, Y.J. Gao, Magnetic force of piezoelectric cantilever energy harvesters with external magnetic field, Eur. Phys. J. 224 (2015) 2839–2853.

[70] Y.G. Leng, D.Tan, J.J. Liu, Y.Y. Zhang, S.B. Fan, Magnetic force analysis and performance of a tri-stable piezoelectric energy harvester under random excitation, J. Sound Vibr. 406 (2017) 146–160.

[71] D. Spreemann, Y. Manoli, Electromagnetic Vibration Energy Harvesting Devices – Archtectures, Design, Modeling and Optimization, Springer, 2012.

[72] G. Akoun, J.P. Yonnet, 3D analytical calculation of the forces exerted between two cuboidal magnets, IEEE Trans, Magn. 20 (1984) 1962–1964.

Table 1 Material properties of magnets.

Item	Material	Remanence Br (T)	Normal coercivity Hcb (kA/m)	Intrinsic coercivity Hcj (kA/m)	Mass energy product BH (kJ/m^3)
Magnets	NdFeB N35	1.17	868	955	279

Table 2 Material parameters and geometry of the hybrid energy harvester.

Parameters	Values
Radius (R_A) and height (h_A) of the moving magnet A	6 mm, 18 mm
Length (l_B), width (w_B) and height (h_B) of the four outer magnets (B1, B2, B3 and B4)	5 mm, 3 mm, 2 mm
Radius (R_C) and height (h_C) of the cylindrical magnets (C1 and C2)	5 mm, 4mm
Distance (R_B) between the center of the four outer magnets (B1, B2, B3 and B4) and the coordinate origin	11.5 mm
Proof mass (m_p)	0.0146 kg
Gravitational constant (g)	9.81 m/s^2
Magnetic permeability (μ_0)	$4\pi\times10^{-7}$ H/m

Table 3 A comparsion study between various electromagnetic-triboelectric energy harvesters.

Approach	Acceleration	Excited frequency	Bandwidth	Peak Power	Power density
Multimodal + Nonlinear stiffening [46]	2g	80 Hz	46–114 Hz	50.2 μW	0.8 W/m^3
Double-deck sandwiched structure for 4 TENG and 2 EMG units [47]	/	22 Hz	/	19.8 mW	167.22 W/m^3
Floating oscillator-embedded structure [48]	1.7g	7.5 Hz	8–12 Hz	/	130W/kg m^3 for TENG and 128W/kg m^3 for EMG
Cantilever structure [50]	2g	20 Hz	10–45 Hz	53 μW (EMG) 30 μW/ m^2 (TENG)	/
Magnetically floated type [51]	0.6g	4.5 Hz	3–5 Hz	10.07 mW	344 W/m^3
Linear tubular EMG unit in conjunction with grating structured freestanding mode TENG [52]	2.5g	5 Hz	1–6 Hz	/	120 W/m^3
Present work (Magnetic levitation + Tri-stable nonlinearity)	1g	8 Hz	3–8 Hz	6.9 mW (Horizontal orientation)	132 W/m^3

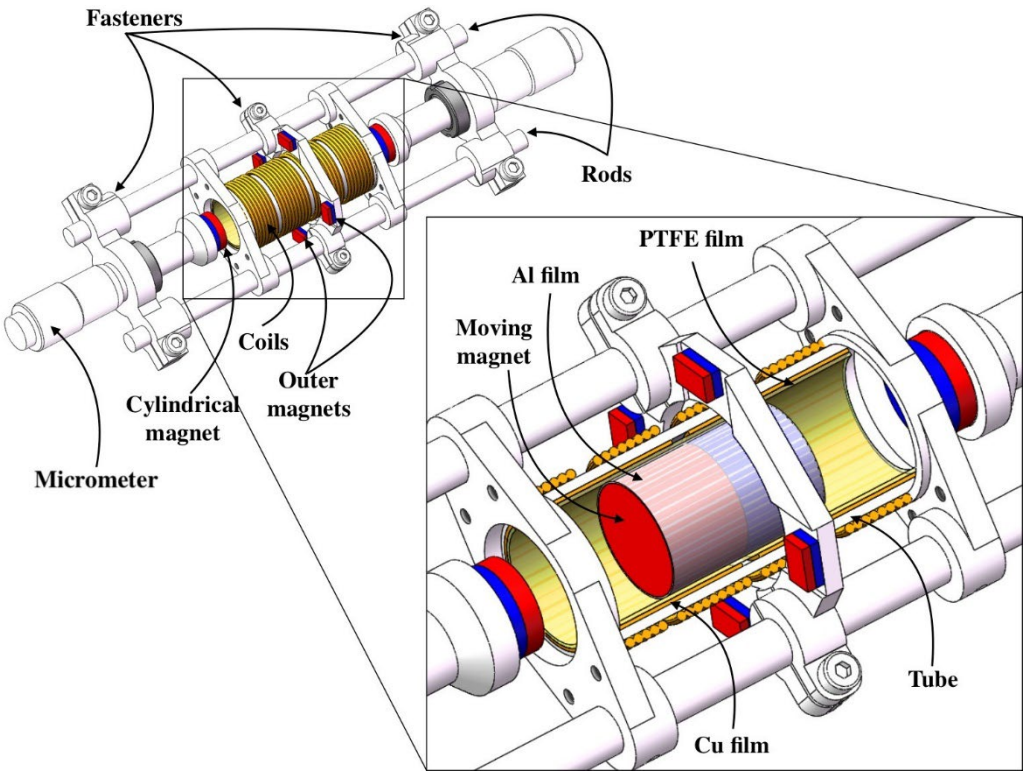

(a)

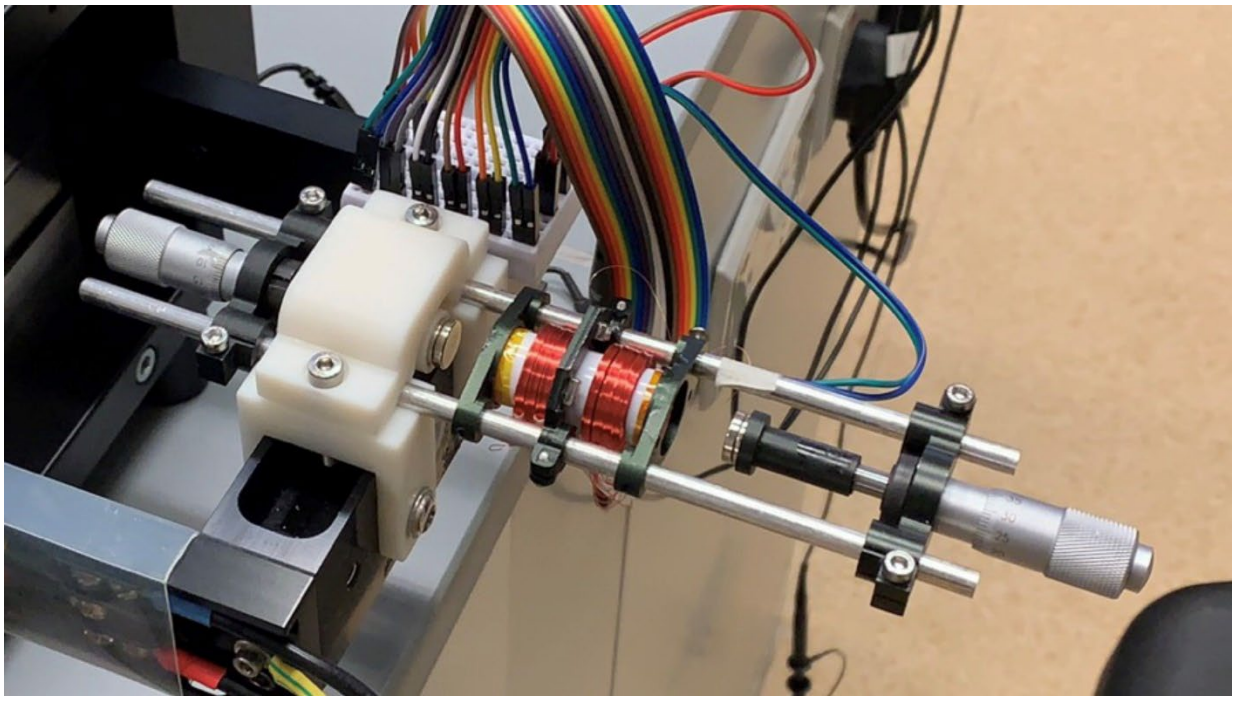

(b)

Fig. 1. (a) Schematic of a novel hybrid energy harvester; and (b) a fabricated prototype.

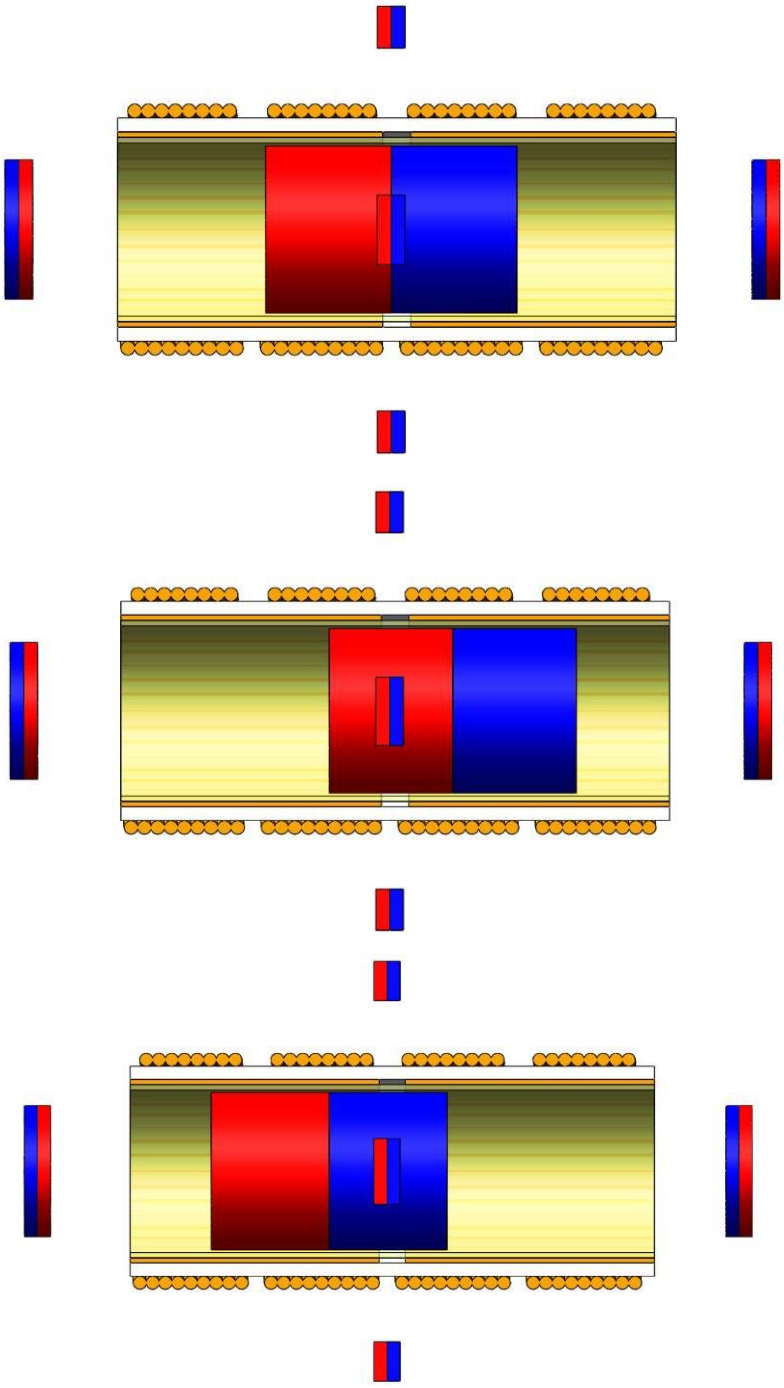

(b)

Fig. 2. Three stable equilibrium positions of the slider in a symmetric tri-stable state.

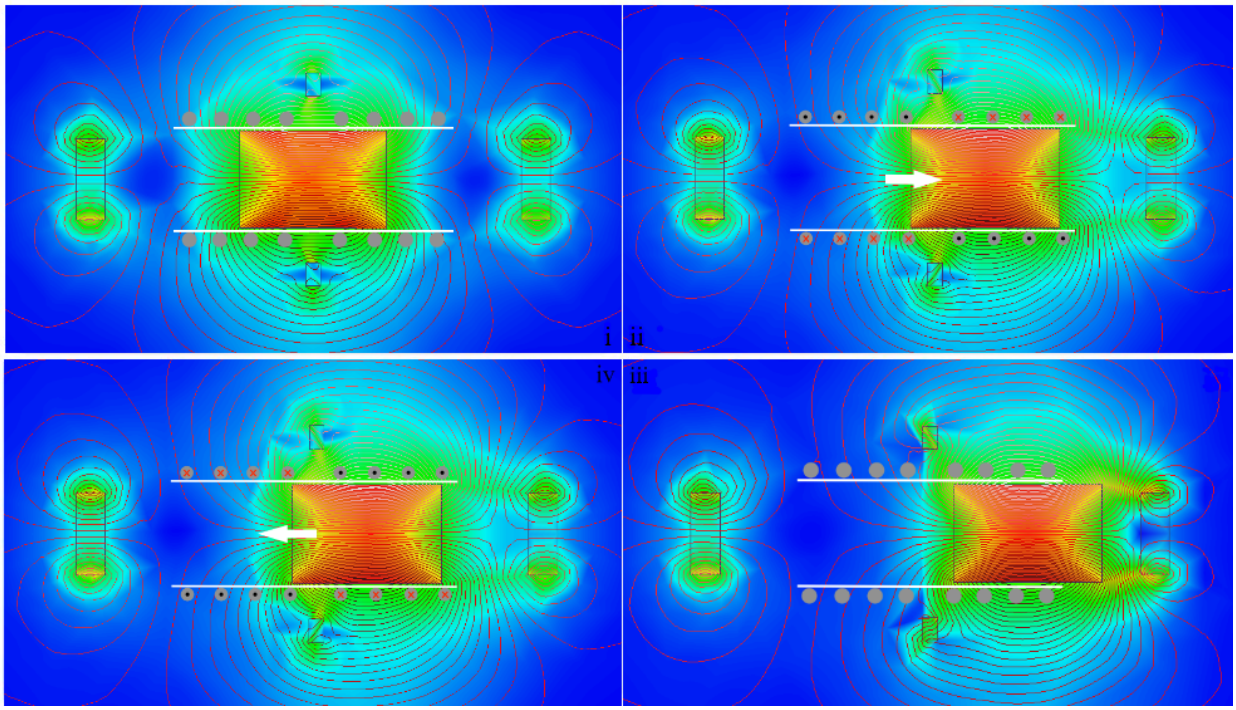

(a)

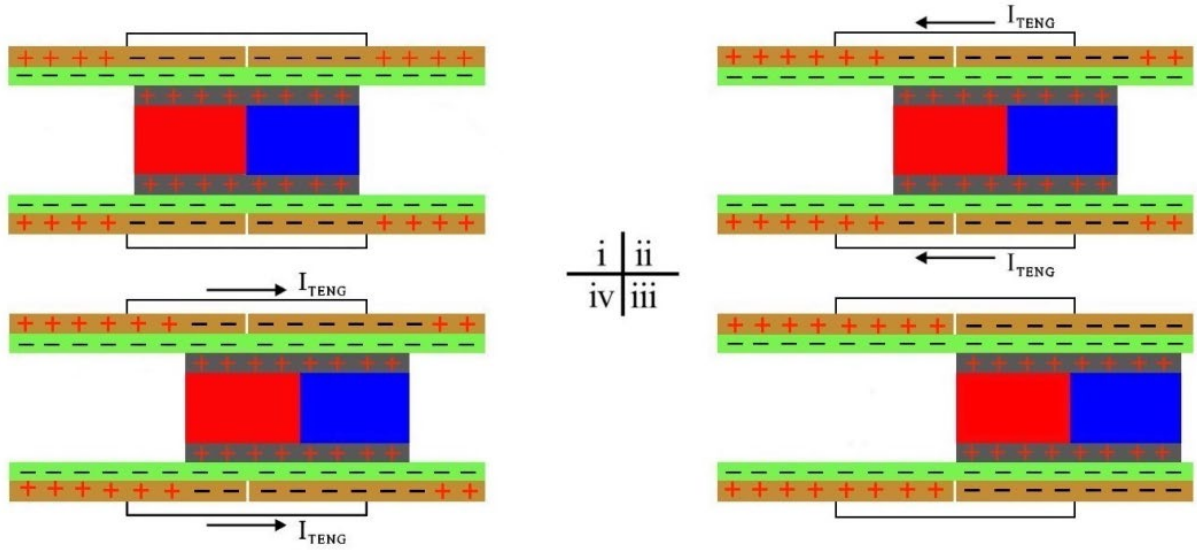

(b)

Fig. 3. Power generation process of (a) the EMG unit and (b) the TENG unit over a half cycle.

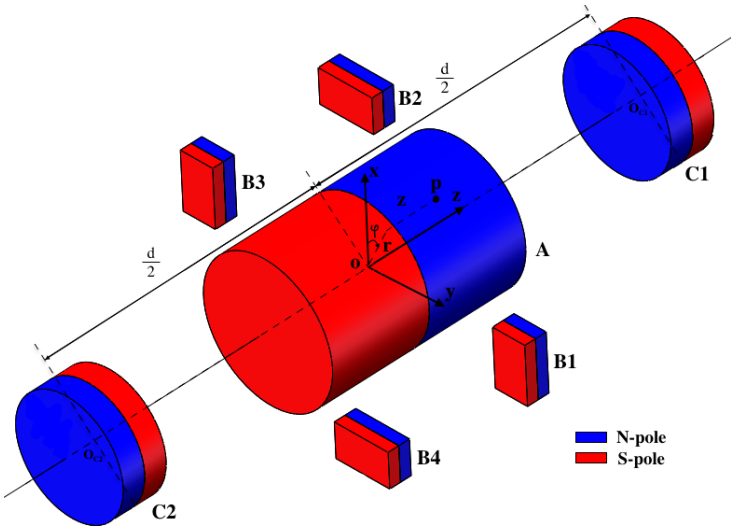

(a)

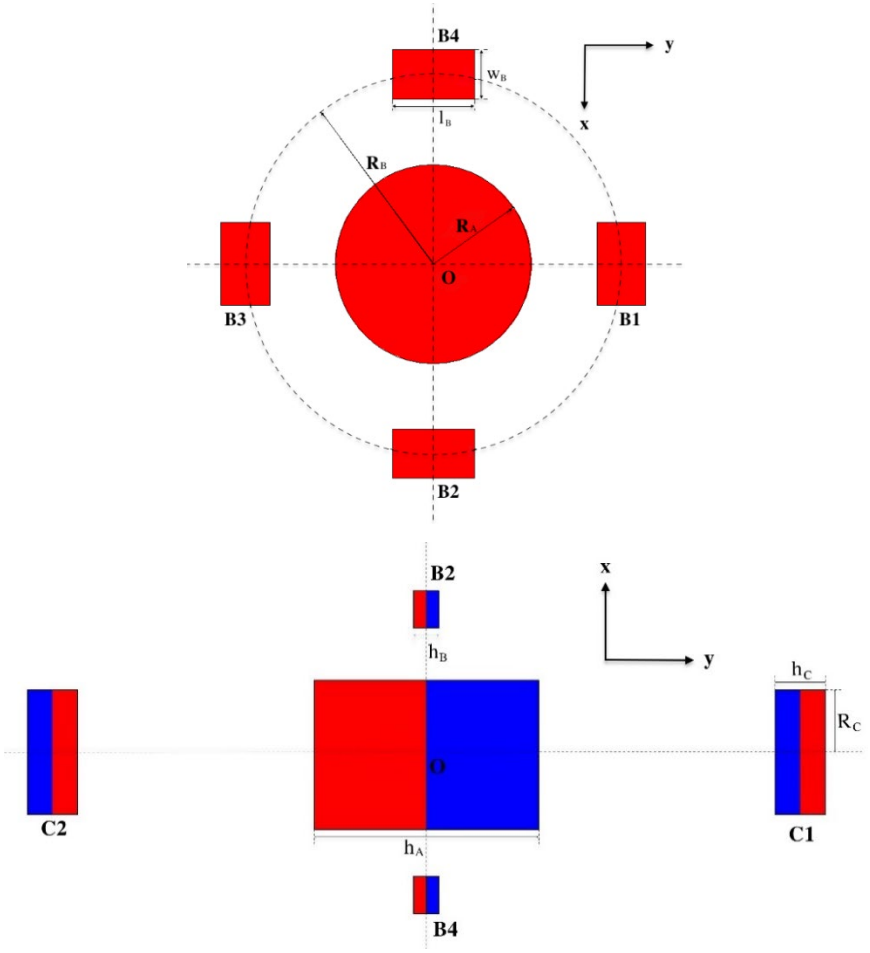

(b)

Fig. 4. (a) Geometric diagram of the magnet model; and (b) cross-sectional views of the magnet model.

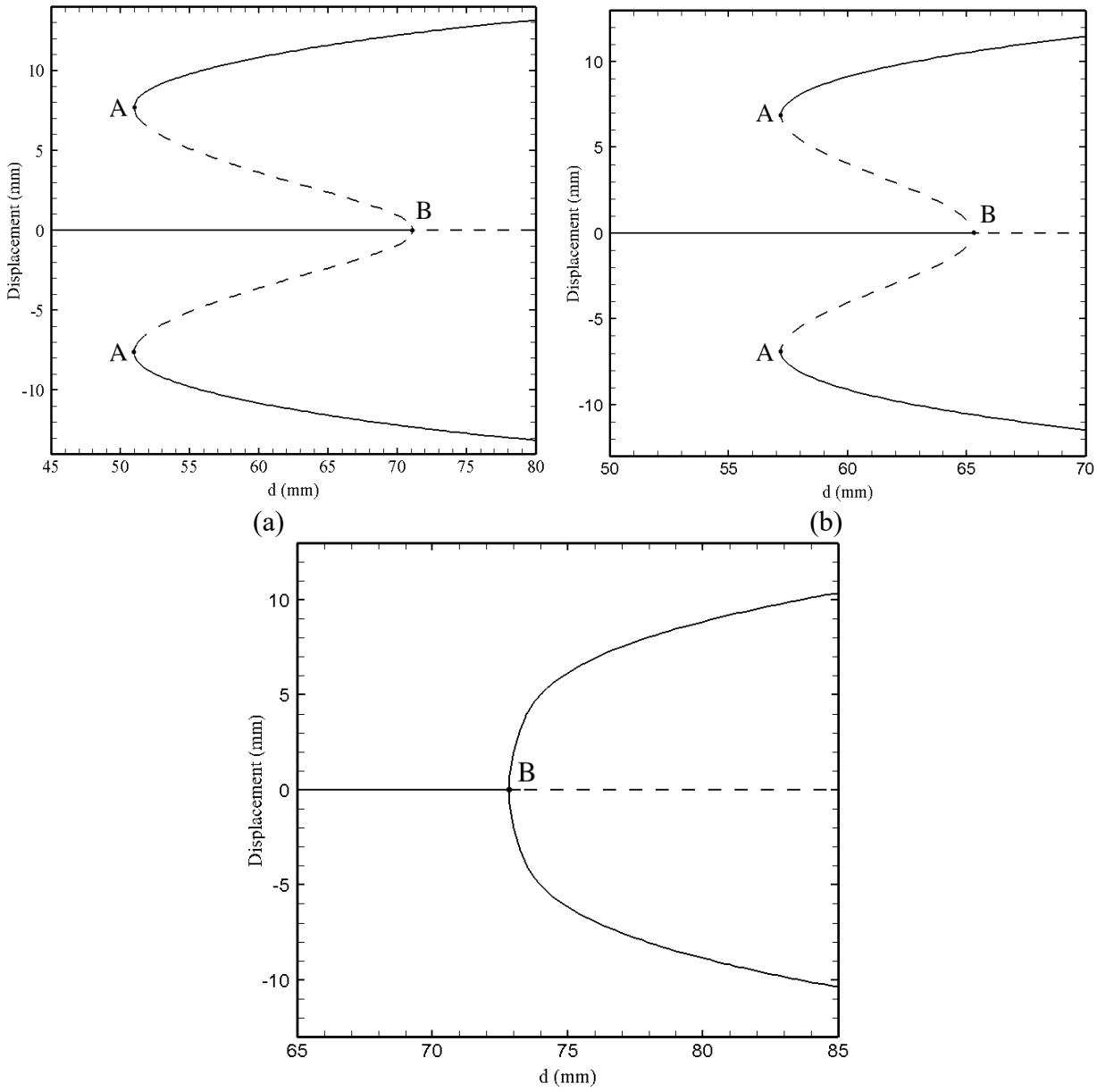

Fig. 5. Bifurcation diagrams of the equilibrium solutions for R_B = (a) 10 mm; (b) 11.5 mm; and (c) 16 mm.

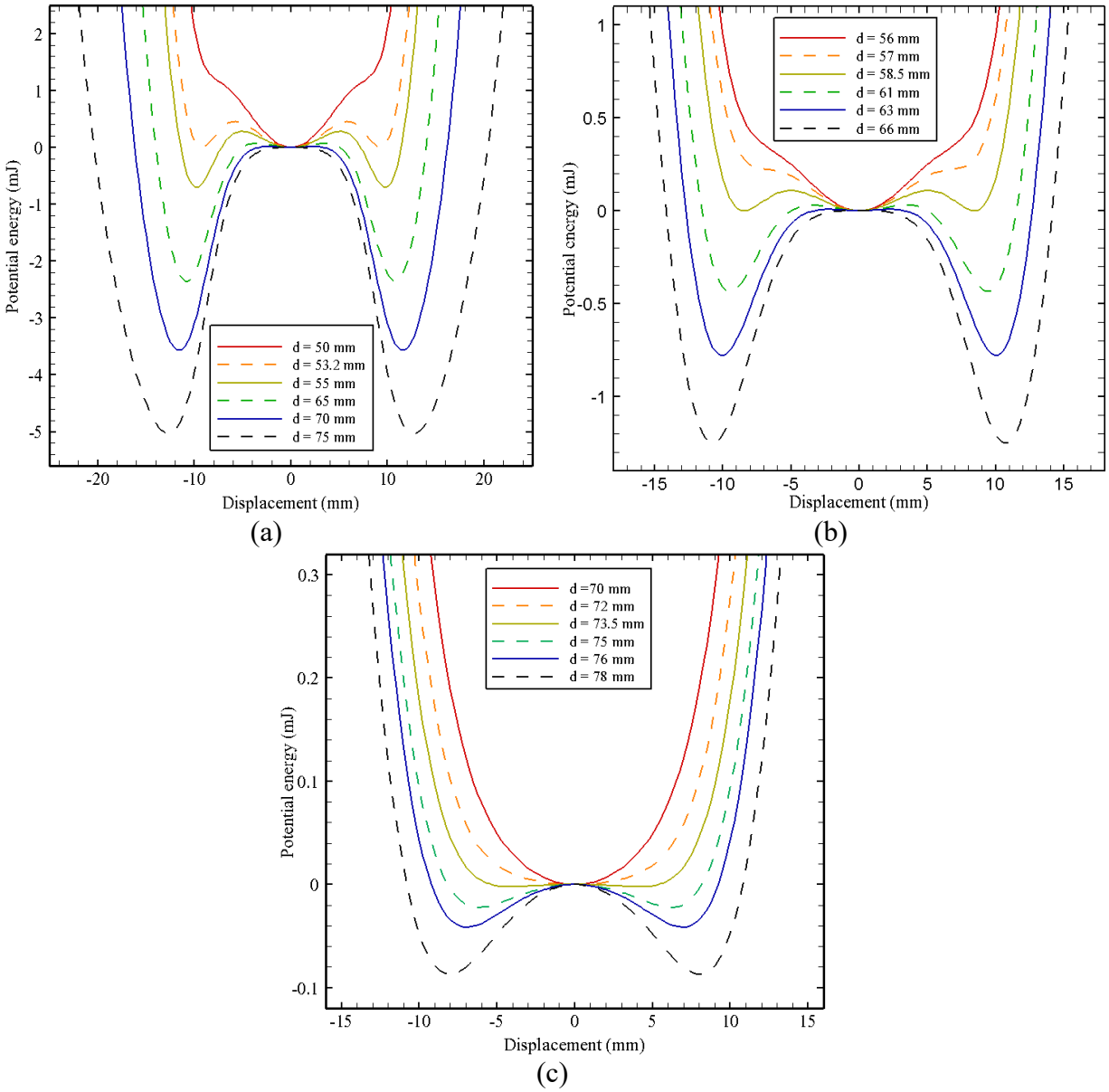

Fig. 6. Variation of potential energy of the symmetric tri-stable system for R_B = (a) 10 mm; (b) 11.5 mm; and (c) 16 mm.

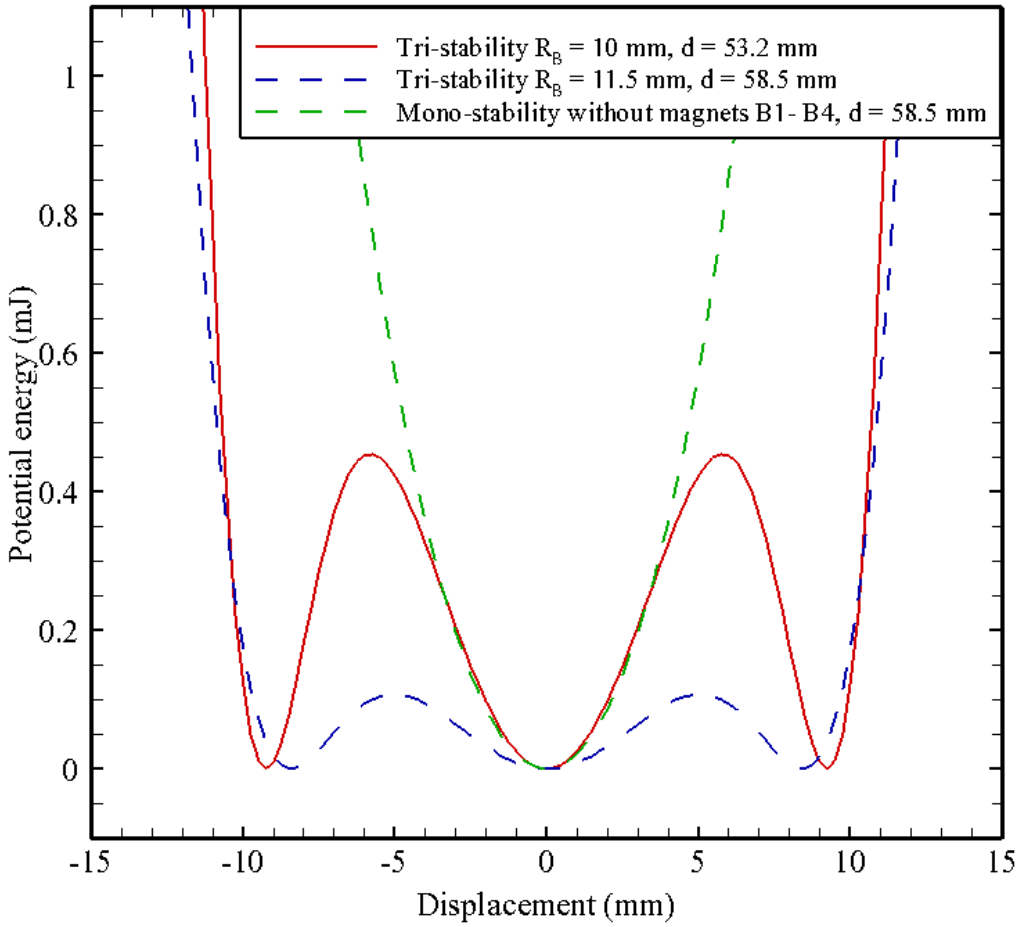

Fig. 7. Potential energy of the tri-stable and mono-stable configurations.

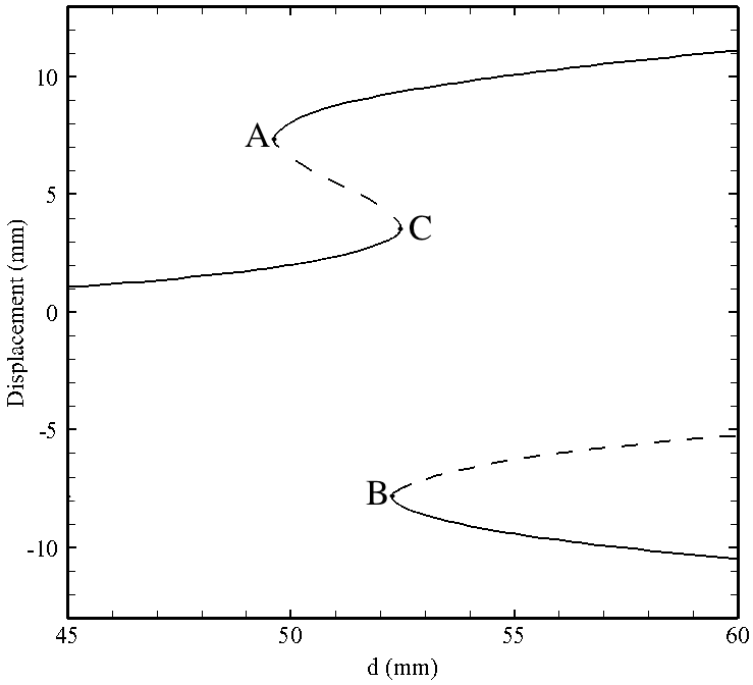

(a)

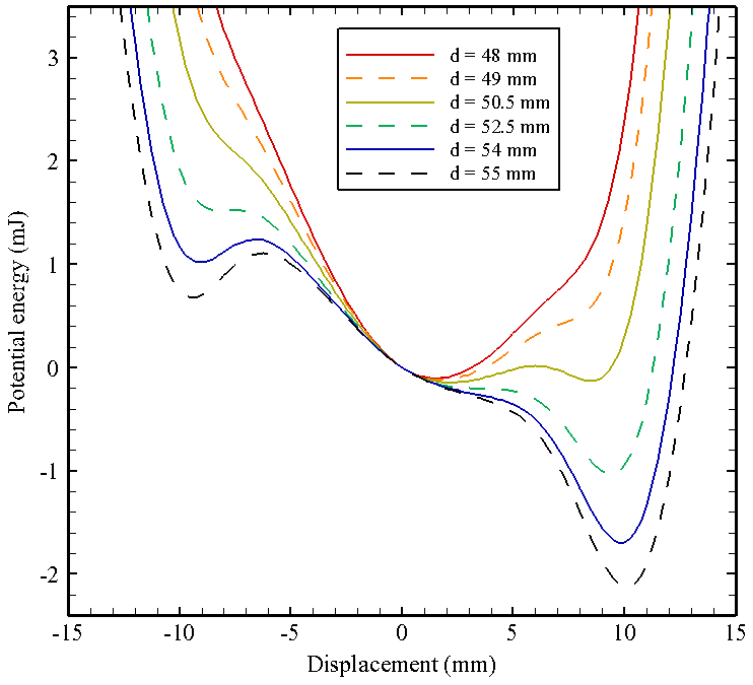

(b)

Fig. 8. (a) Bifurcation diagram of the equilibrium solutions for R_B = 10 mm; and (b) variation of potential energy of the asymmetric tri-stable system for R_B = 10 mm.

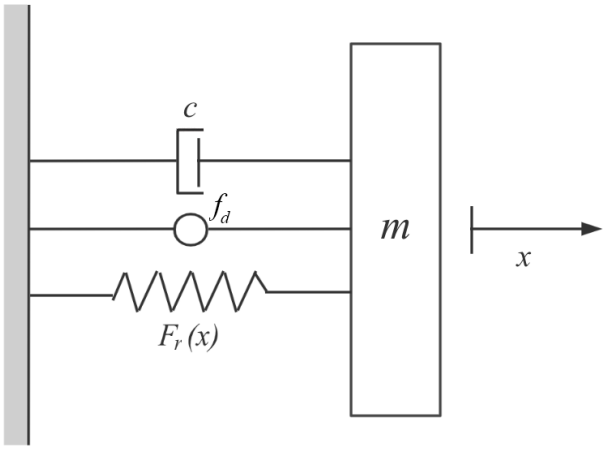

(a)

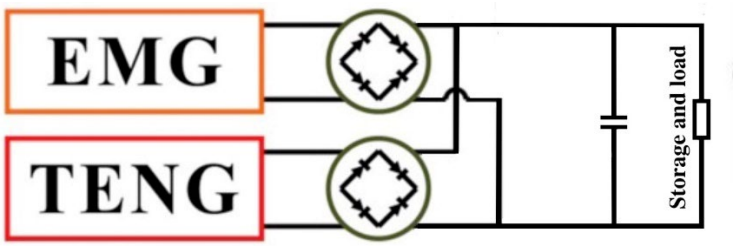

(b)

Fig. 9. (a) A lumped parameter model of the hybrid energy harvester; and (b) a schematic circuit of the hybrid energy harvester.

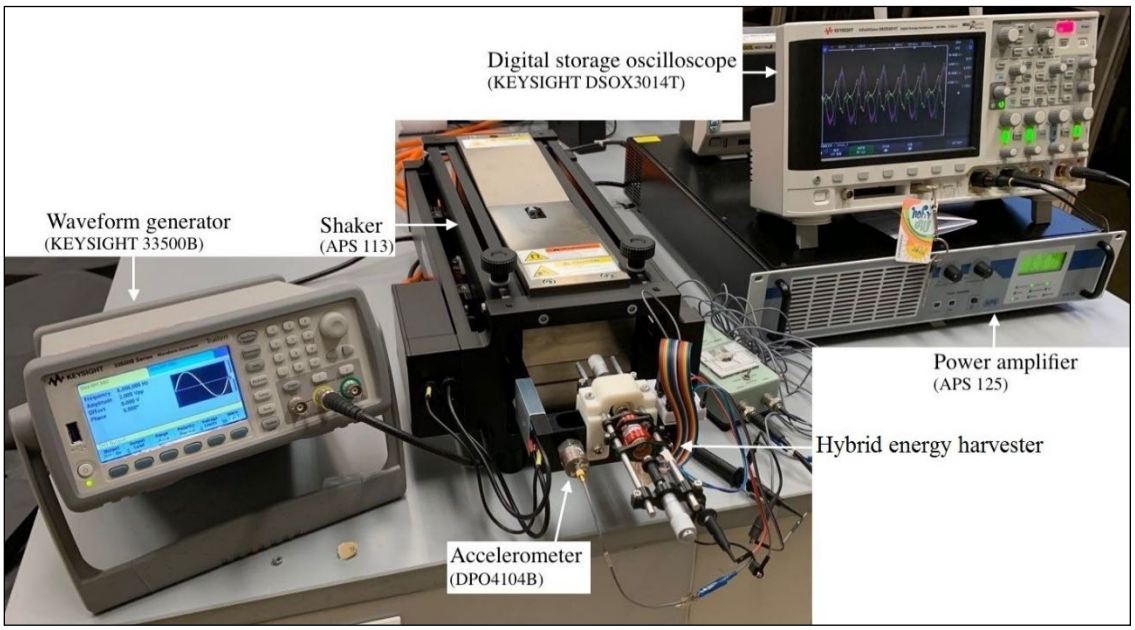

(a)

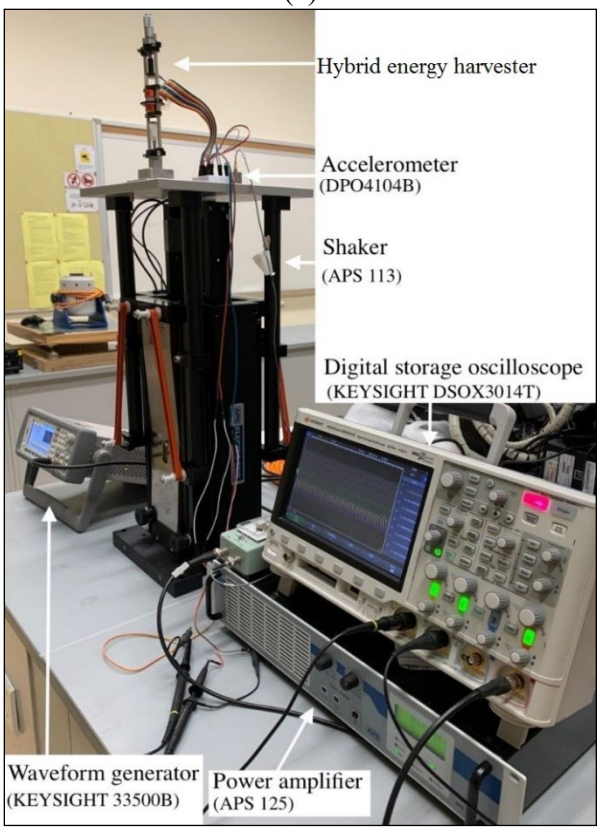

(b)

Fig. 10. Experimental platforms for vibration tests in (a) horizontal direction; and (b) vertical position.

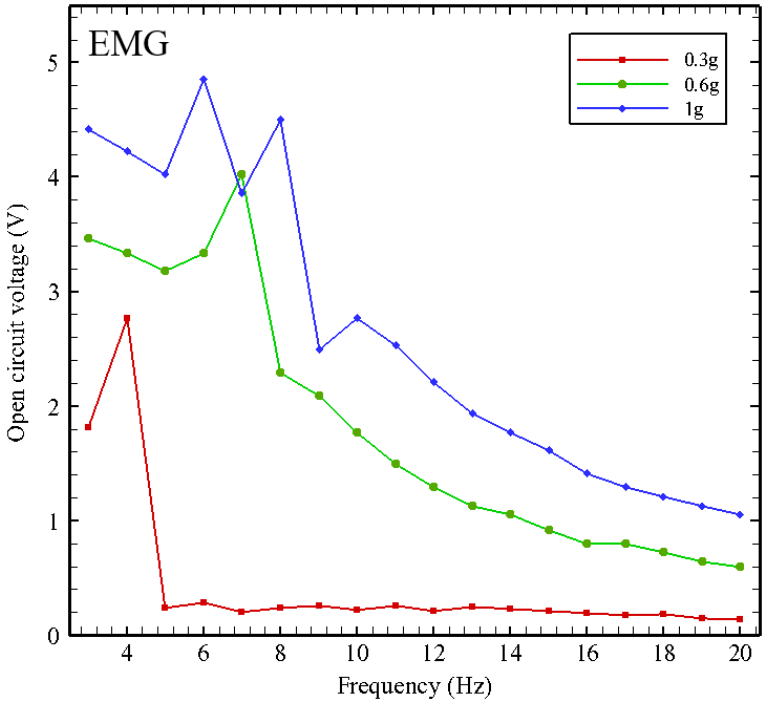

(a)

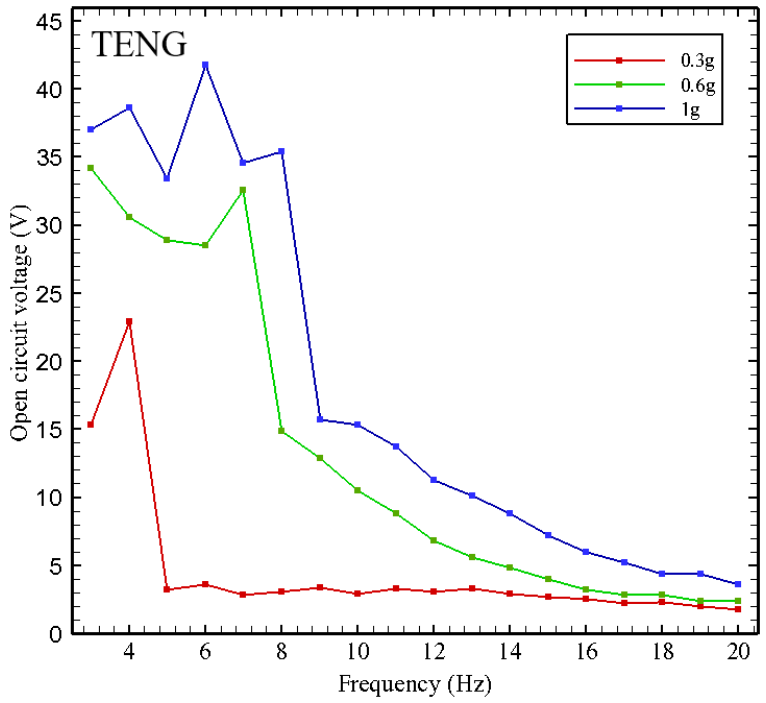

(b)

Fig. 11. Measured open-circuit voltages of the tri-stable system under various acceleration levels (0.3g, 0.6g and 1g): (a) EMG and (b) TENG.

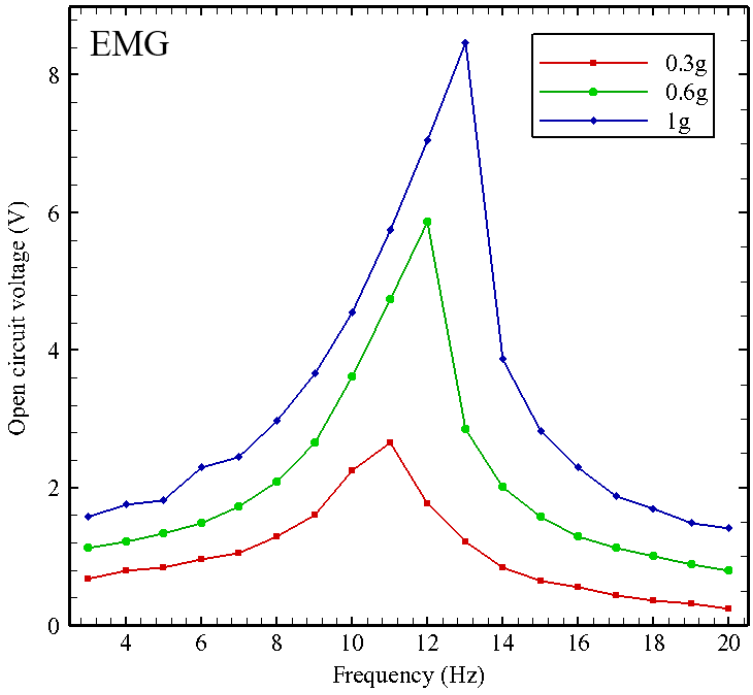

(a)

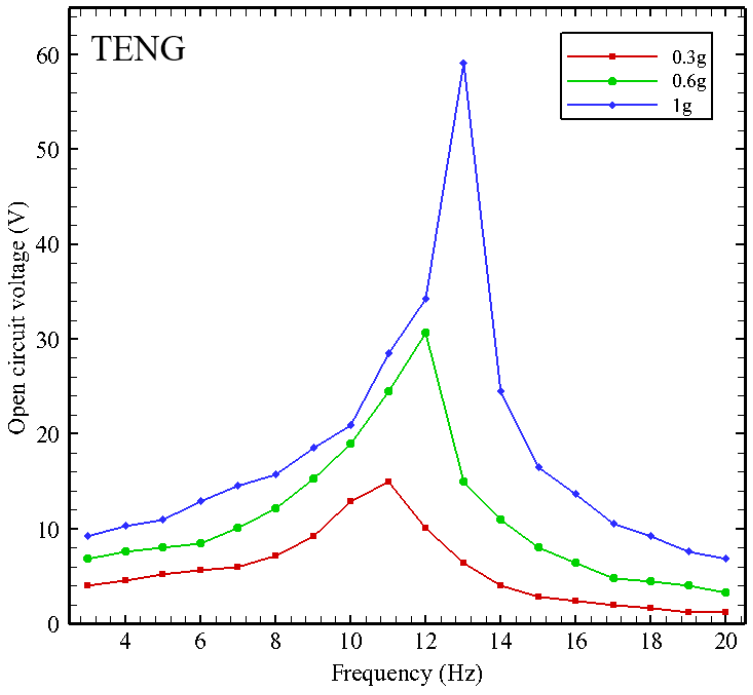

(b)

Fig. 12. Measured open-circuit voltages of the mono-stable system under various acceleration levels (0.3g, 0.6g and 1g): (a) EMG and (b) TENG.

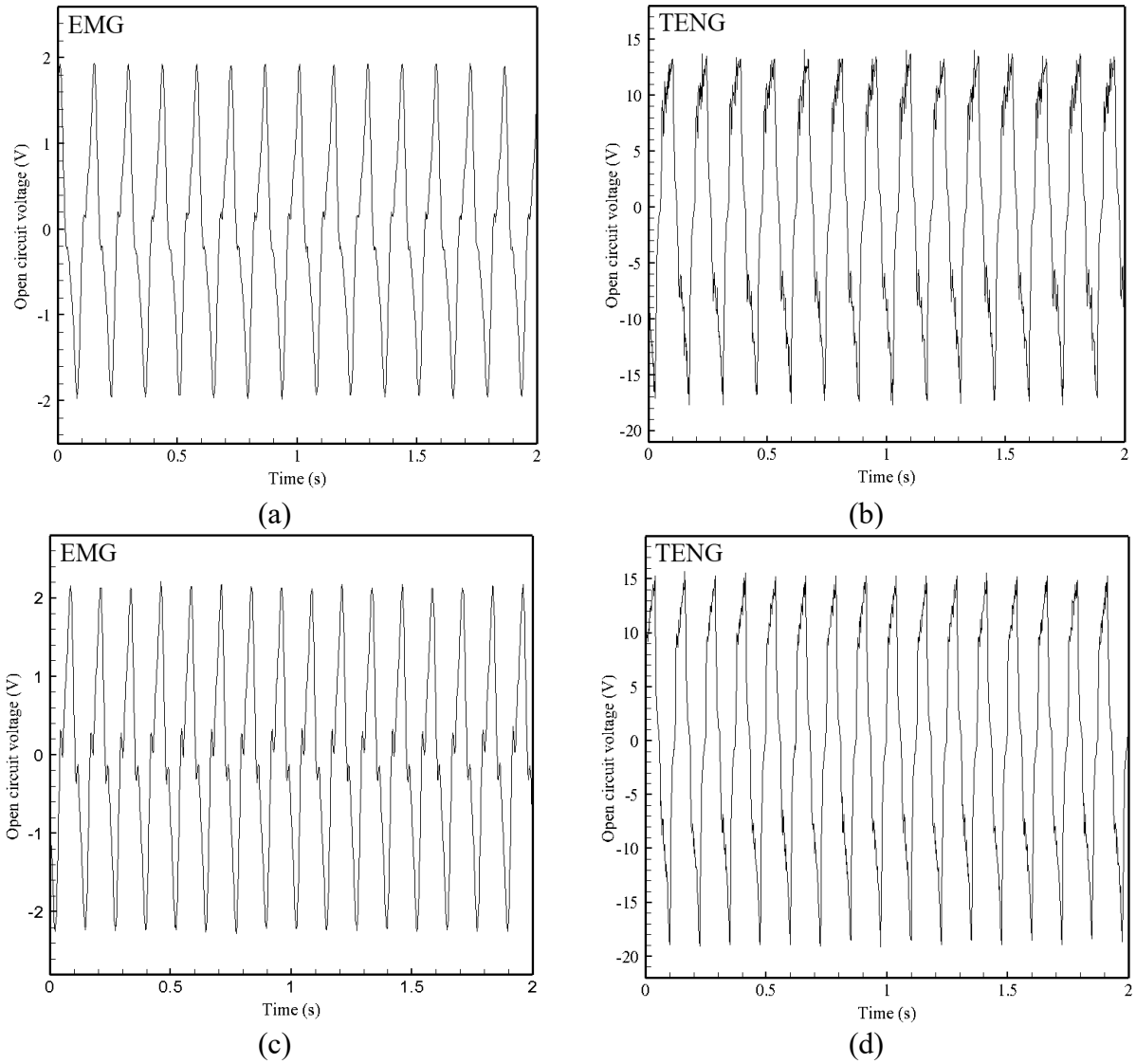

Fig. 13. Measured peak-to-peak open-circuit voltage curves of the tri-stable system: (a) EMG under 7 Hz at 0.6g; (b) TENG under 7 Hz at 0.6g; (c) EMG under 8 Hz at 1g; and (d) TENG under 8 Hz at 1g.

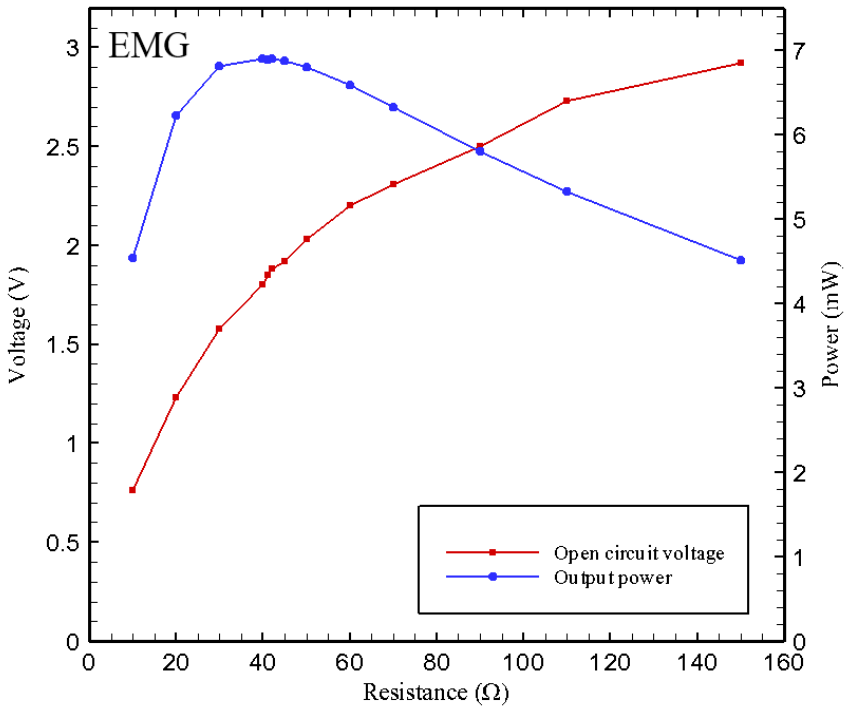

(a)

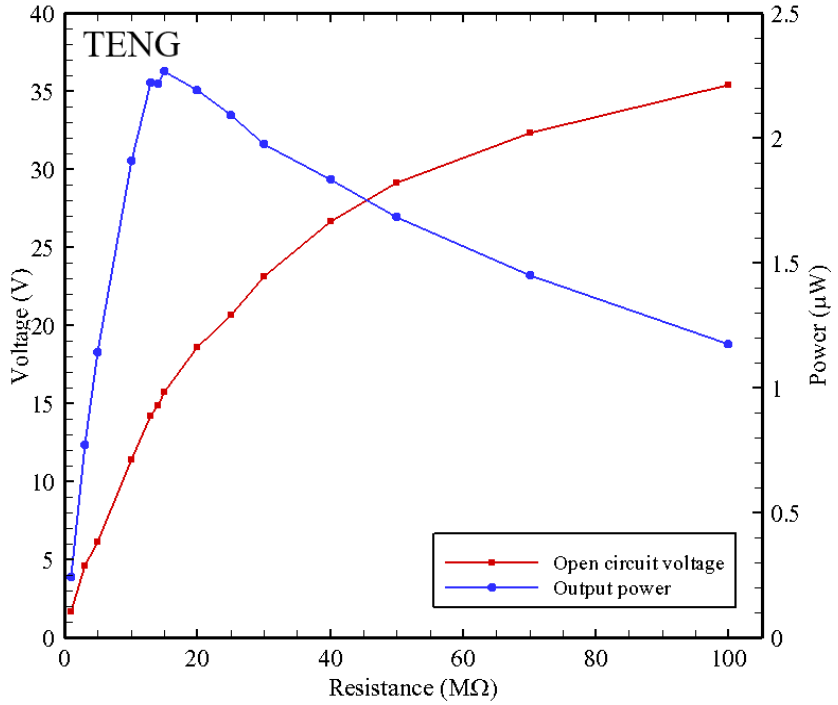

(b)

Fig. 14. Dependence of the open circuit voltage and peak output power on the external load resistance in the tri-stable system: (a) EMG and (b) TENG.

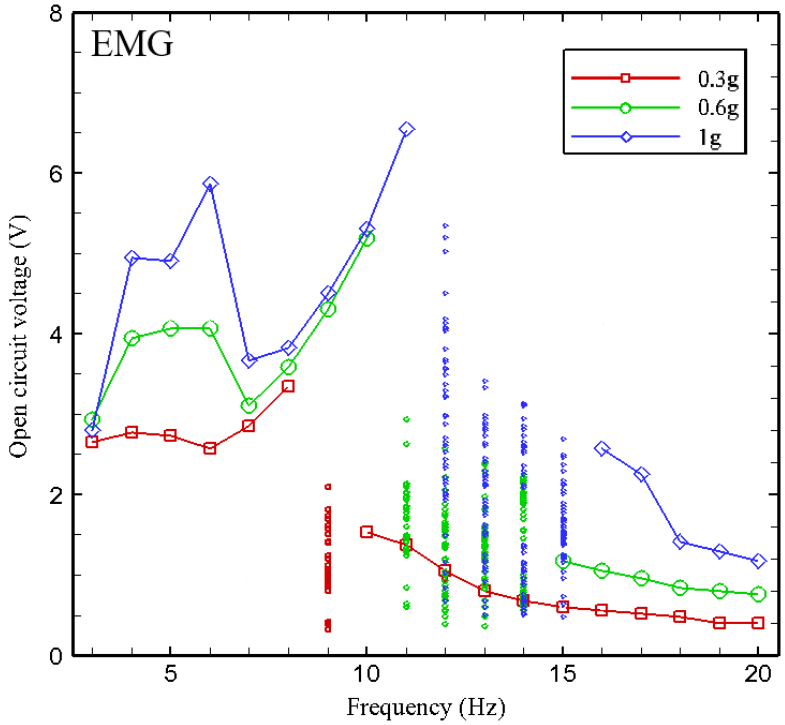

(a)

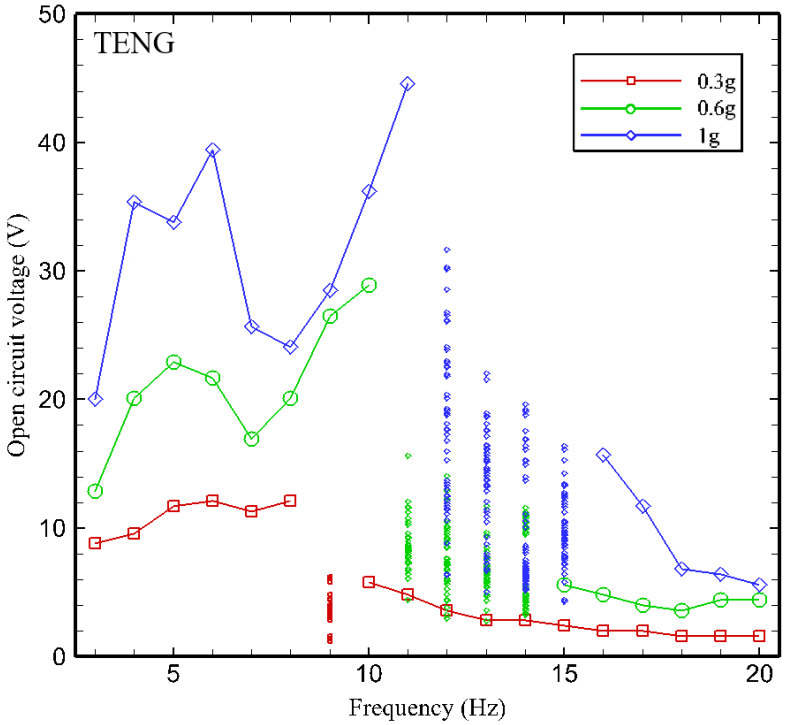

(b)

Fig. 15. Measured open-circuit voltages of the bi-stable system under various acceleration levels (0.3g, 0.6g, and 1g): (a) EMG and (b) TENG.

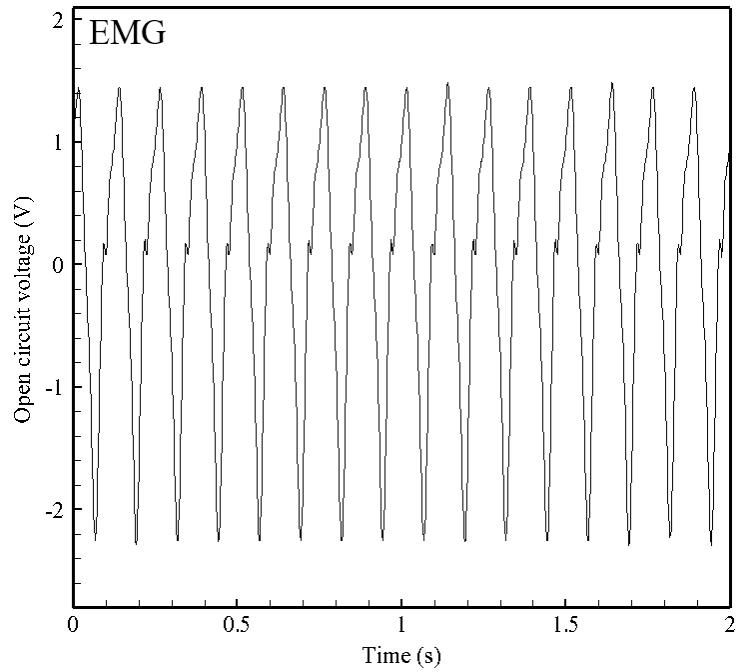

(a)

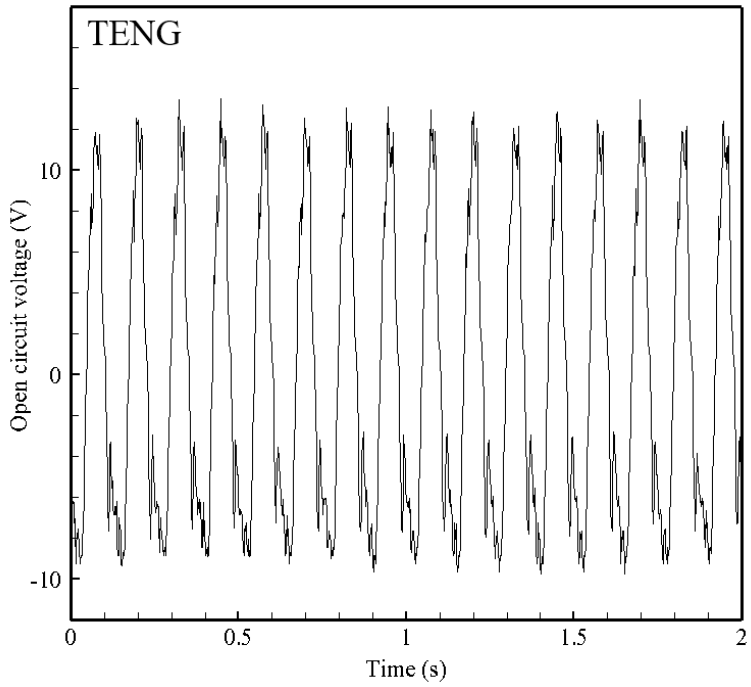

(b)

Fig. 16. Measured open-circuit voltages of the bi-stable system under 8 Hz at 1g: (a) EMG and (b) TENG.

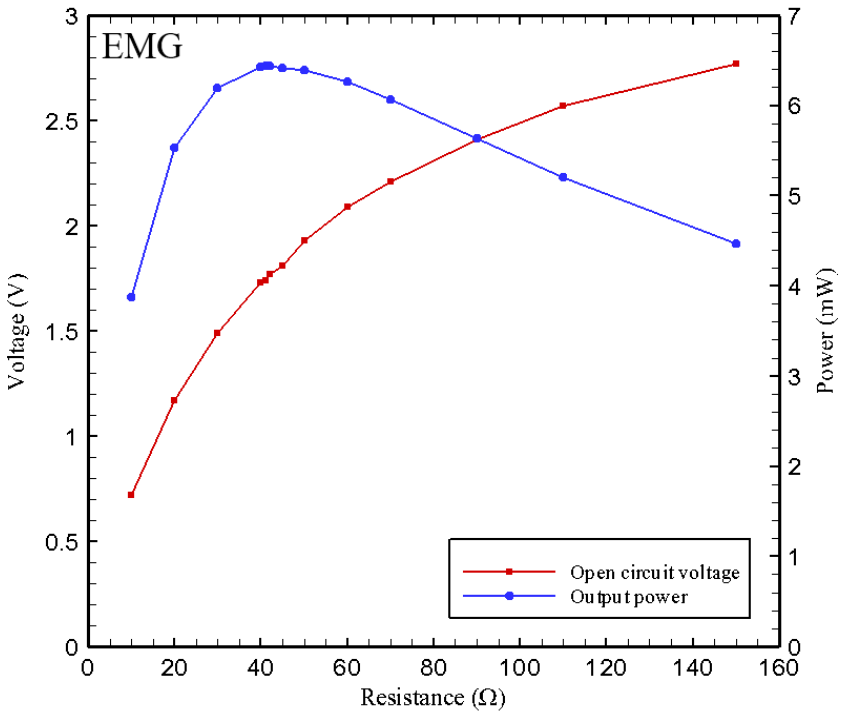

(a)

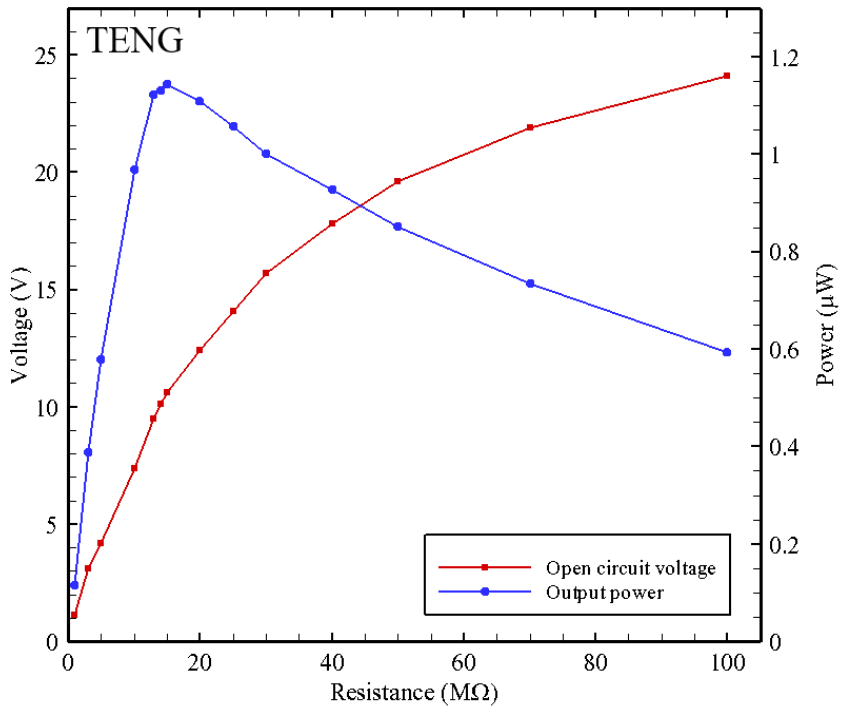

(b)

Fig. 17. Dependence of the open circuit voltage and peak output power on the external load resistance in the bi-stable system: (a) EMG and (b) TENG.

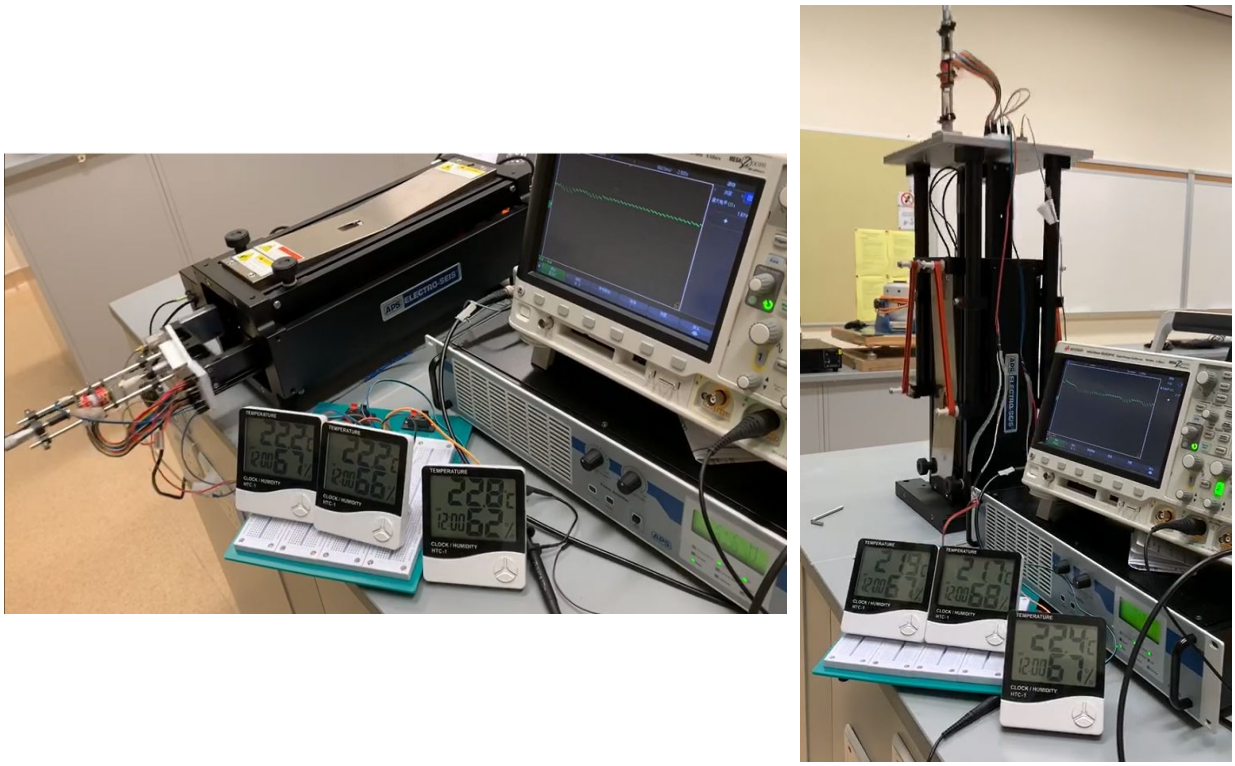

Fig. 18. Demonstration of the hybrid energy harvester for powering three electronic meters simultaneously in both horizontal and vertical orientations under 8 Hz and 1g.